

This is an Open Access document downloaded from ORCA, Cardiff University's institutional repository:<https://orca.cardiff.ac.uk/id/eprint/104690/>

This is the author's version of a work that was submitted to / accepted for publication.

Citation for final published version:

Bakx, Tom, Eales, Stephen , Negrello, Mattia , Smith, Matthew , Valiante, Elisabetta, Holland, W. S., Baes, M., Bourne, N., Clements, D. L., Dannerbauer, H., De Zotti, G., Dunne, Loretta , Dye, S., Furlanetto, C., Ivison, R. J., Maddox, Steve , Marchetti, L., Michałowski, M. J., Omont, A., Oteo, I., Wardlow, J. L., Werf, P. van der and Yang, C. 2018. The Herschel Bright Sources (HerBS): sample definition and SCUBA-2 observations. *Monthly Notices of the Royal Astronomical Society* 473 (2) , pp. 1751-1773.  
10.1093/mnras/stx2267

Publishers page: <http://dx.doi.org/10.1093/mnras/stx2267>

Please note:

Changes made as a result of publishing processes such as copy-editing, formatting and page numbers may not be reflected in this version. For the definitive version of this publication, please refer to the published source. You are advised to consult the publisher's version if you wish to cite this paper.

This version is being made available in accordance with publisher policies. See <http://orca.cf.ac.uk/policies.html> for usage policies. Copyright and moral rights for publications made available in ORCA are retained by the copyright holders.



## The *Herschel* Bright Sources (HerBS): Sample definition and SCUBA-2 observations.

Tom J. L. C. Bakx<sup>1\*</sup>, S. A. Eales<sup>1</sup>, M. Negrello<sup>1</sup>, M. W. L. Smith<sup>1</sup>, E. Valiante<sup>1</sup>,  
W. S. Holland<sup>2</sup>, M. Baes<sup>3</sup>, N. Bourne<sup>4</sup>, D. L. Clements<sup>5</sup>, H. Dannerbauer<sup>6,20,21</sup>,  
G. De Zotti<sup>7</sup>, L. Dunne<sup>1</sup>, S. Dye<sup>8</sup>, C. Furlanetto<sup>8,9</sup>, R. J. Ivison<sup>4,10</sup>, S. Maddox<sup>1</sup>,  
L. Marchetti<sup>11</sup>, M. J. Michałowski<sup>4,19</sup>, A. Omont<sup>12,13</sup>, I. Oteo<sup>4,10</sup>, J. L. Wardlow<sup>14</sup>,  
P. van der Werf<sup>15</sup> and C. Yang<sup>12,13,16,17,18</sup>.

<sup>1</sup>*School of Physics & Astronomy, Cardiff University, The Parade, Cardiff, CF24 3AA UK*

<sup>2</sup>*UK Astronomy Technology Centre, Royal Observatory, Blackford Hill, Edinburgh EH9 3HJ, UK*

<sup>3</sup>*Sterrenkundig Observatorium, Universiteit Gent, Krijgslaan 281 S9, B-9000 Gent, Belgium*

<sup>4</sup>*Institute for Astronomy, University of Edinburgh, Royal Observatory, Edinburgh EH9 3HJ, UK*

<sup>5</sup>*Astrophysics Group, Imperial College, Blackett Laboratory, Prince Consort Road, London SW7 2AZ, UK*

<sup>6</sup>*Universität Wien, Institut für Astrophysik, Türkenschanzstrabe 17, 1180 Wien, Austria*

<sup>7</sup>*INAF-Osservatorio Astronomico di Padova, Vicolo dell'Osservatorio 5, I-35122 Padova, Italy*

<sup>8</sup>*School of Physics and Astronomy, University of Nottingham, University Park, Nottingham NG7 2RD, UK*

<sup>9</sup>*CAPES Foundation, Ministry of Education of Brazil, Brasília/DF, 70040-020, Brazil*

<sup>10</sup>*European Southern Observatory, Karl-Schwarzschild-Strasse 2, 85748 Garching bei München, Germany*

<sup>11</sup>*Department of Physical Science, The Open University, Milton Keynes MK7 6AA, UK*

<sup>12</sup>*UPMC Univ. Paris 06, UMR7095, Institut d'Astrophysique de Paris, 75014 Paris, France*

<sup>13</sup>*CNRS, UMR7095, Institut d'Astrophysique de Paris, 75014 Paris, France*

<sup>14</sup>*Centre for Extragalactic Astronomy, Department of Physics, Durham University, South Road, Durham, DH1 3LE, UK*

<sup>15</sup>*Leiden Observatory, Leiden University, P.O. Box 9513, NL - 2300 Leiden, The Netherlands*

<sup>16</sup>*Purple Mountain Observatory/Key Lab of Radio Astronomy, Chinese Academy of Sciences, Nanjing 210008, PR China*

<sup>17</sup>*Institut d'Astrophysique Spatiale, CNRS, Univ. Paris-Sud, Université Paris-Saclay, BÂt. 121, 91405 Orsay Cedex, France*

<sup>18</sup>*Graduate University of the Chinese Academy of Sciences, 19A Yuquan Road, Shijingshan District, 10049, Beijing, PR China*

<sup>19</sup>*Astronomical Observatory Institute, Faculty of Physics, Adam Mickiewicz University, ul. Słoneczna 36, 60-286 Poznań, Poland*

<sup>20</sup>*Instituto de Astrofísica de Canarias (IAC), E-38205 La Laguna, Tenerife, Spain*

<sup>21</sup>*Universidad de La Laguna, Dpto. Astrofísica, E-38206 La Laguna, Tenerife, Spain*

Accepted XXX. Received YYY; in original form ZZZ

### ABSTRACT

We present the *Herschel* Bright Sources (HerBS) sample, a sample of bright, high-redshift *Herschel* sources detected in the 616.4 square degree H-ATLAS survey. The HerBS sample contains 209 galaxies, selected with a 500  $\mu\text{m}$  flux density greater than 80 mJy and an estimated redshift greater than 2. The sample consists of a combination of HyLIRGs and lensed ULIRGs during the epoch of peak cosmic star formation. In this paper, we present SCUBA-2 observations at 850  $\mu\text{m}$  of 189 galaxies of the HerBS sample, 152 of these sources were detected. We fit a spectral template to the *Herschel*-SPIRE and 850  $\mu\text{m}$  SCUBA-2 flux densities of 22 sources with spectroscopically determined redshifts, using a two-component modified blackbody spectrum as a template. We find a cold- and hot-dust temperature of  $21.29^{+1.35}_{-1.66}$  K and  $45.80^{+2.88}_{-3.48}$  K, a cold-to-hot dust mass ratio of  $26.62^{+5.61}_{-6.74}$  and a  $\beta$  of  $1.83^{+0.14}_{-0.28}$ . The poor quality of the fit suggests that the sample of galaxies is too diverse to be explained by our simple model. Comparison of our sample to a galaxy evolution model indicates that the fraction of lenses is high. Out of the 152 SCUBA-2 detected galaxies, the model predicts  $128.4 \pm 2.1$  of those galaxies to be lensed (84.5%). The SPIRE 500  $\mu\text{m}$  flux suggests that out of all 209 HerBS sources, we expect  $158.1 \pm 1.7$  lensed sources, giving a total lensing fraction of 76 per cent.

**Key words:** submillimetre: galaxies - galaxies: high-redshift - gravitational lensing: strong

### 1 INTRODUCTION

The *Herschel* Space Observatory (Pilbratt et al. 2010) has increased the number of known sub-millimetre galaxies (SMGs)

\* E-mail: bakxtj@cardiff.ac.uk (Cardiff)

from hundreds to hundreds of thousands. The H-ATLAS survey (*Herschel* Astrophysical Terahertz Large Area Survey - [Eales et al. 2010](#); [Valiante et al. 2016](#)) is one of the largest legacies of *Herschel*. This survey observed a total of 616.4 square degrees over five fields in five wavebands. The large-area surveys done with *Herschel* allow us to select sources that are among the brightest in the sky, of which a large percentage are lensed ULIRGs (Ultra-Luminous Infrared Galaxies,  $10^{12} L_{\odot} < L_{\text{FIR}} < 10^{13} L_{\odot}$ ) and HyLIRGs (Hyper-Luminous Infrared Galaxy,  $L_{\text{FIR}} > 10^{13} L_{\odot}$ ) at high redshift.

A similar selection for bright sources was already exploited in the 14.4 sq. deg. Science Demonstration Phase (SDP) of H-ATLAS by [Negrello et al. \(2010\)](#), who used a simple flux cut-off to select lensed sources. They were able to remove all contaminants from their selection, local galaxies and blazars, and identified five lensed galaxies. [Wardlow et al. \(2013\)](#) followed a similar approach on the 94 sq. deg. HerMES (*Herschel* Multi-tiered Extragalactic Survey) maps, and selected 13 sources with  $S_{500\mu\text{m}} > 100\text{mJy}$ . Nine of these sources had follow-up data, done with the Sub-Millimetre Array (SMA), the Hubble Space Telescope (HST), Jansky Very Large Array (JVLA), Keck, and Spitzer. [Wardlow et al. \(2013\)](#) combined these data for six sources and confirmed their lensing nature, while three other sources had their lensing nature already confirmed by [Borys et al. \(2006\)](#), [Conley et al. \(2011\)](#), and [Ikarashi et al. \(2011\)](#). Recently, [Negrello et al. \(2017\)](#) and [Nayyeri et al. \(2016\)](#) used the same  $S_{500\mu\text{m}} > 100\text{mJy}$  flux density cut-off on the full H-ATLAS (616.4 sq. deg.) and HeLMS (372 sq. deg.) maps, and created samples containing 77 and 80 sources, respectively. Spectroscopic and optical follow-up observations were able, so far, to confirm that 20 sources are indeed lensed, one is a proto-cluster ([Iverson et al. 2013](#)), while the remaining sources in [Negrello et al. \(2017\)](#) await more observations to be carried out to confirm their nature.

Large samples of lensed sources are interesting, both because of the lensed source and the intervening lensing galaxy ([Treu 2010](#)). The lensed source has an amplified flux density and increased angular size. The amplification in flux density allows us to study sources that would otherwise be too faint to detect. The increase in angular size allows us to study the internal properties of high redshift sources with high resolution sub-mm/mm and radio observatories, such as ALMA (Atacama Large Millimeter Array) and the VLA (Very Large Array). As most intervening, lensing sources are passively evolving ellipticals, they are sub-mm dim and their contribution to the total measured flux density is minimal. This allowed [ALMA Partnership \(2015\)](#), [Dye et al. \(2015\)](#), [Hatsukade et al. \(2015\)](#), [Rybak et al. \(2015\)](#), [Swinbank et al. \(2015\)](#) and [Tamura et al. \(2015\)](#) to study SDP.81 down to sub-kiloparsec scales, using the increase in angular size in order to resolve the morphological and dynamical properties of a galaxy at a redshift of 3.

Sub-mm detected lensed sources, similar to SDP.81, are forming stars at rates of hundreds to several thousands of solar masses per year, and large samples of them can allow statistically significant studies into these extremely star-forming sources. This is important, because the comoving density of ULIRGs at  $z = 2$  to 4 is about a thousand times greater than in the local universe, and these dusty star-forming galaxies are estimated to contribute about 10% of the total star formation in this redshift range ([Hughes et al. 1998](#); [Blain et al. 1999](#); [Smail et al. 2002](#); [Wardlow et al. 2011](#); [Casey et al. 2014](#)). This means that SMGs contribute significantly to the peak in cosmic star formation, which occurred around  $z \sim 2.3$  ([Chapman et al. 2005](#)).

While the star-formation rate of the universe has been measured up to redshift  $z \sim 8$  in rest-frame UV surveys, these studies only measure the unobscured star-formation rates ([Madau & Dickinson 2014](#)). The star formation processes in these dusty star-forming galaxies (DSFGs) tend to be obscured by the dust, and are missed by current optical investigations of the cosmic star-formation rate. An added benefit of using sub-mm observations to measure the obscured star-formation rate is that sub-mm flux density falls only slowly with redshift, because of the negative K-correction: sub-mm observations observe the Rayleigh-Jeans part of the modified blackbody spectrum, which causes the flux density to increase as the galaxy's redshift increases. This increase is able to compensate for the cosmological dimming due to the increase of luminosity distance, e.g. a redshift 1 or 4 galaxy has a similar flux density in sub-mm wavelengths ([Blain & Longair 1993](#); [Blain et al. 2002](#); [Betherton et al. 2015](#)).

The foreground galaxy's total mass (dark and baryonic) distribution determines the lensed morphology of the sub-mm detected system [Vegetti et al. \(2012\)](#); [Hezaveh et al. \(2016a,b\)](#). Therefore, high-resolution imaging of the lensed morphology allows the detection of low-mass substructures in lensing galaxies. These substructures can then be used to test the formation of structure in large-scale cosmological simulations, such as the Millennium ([Springel et al. 2005](#)) and the recent Eagle simulation ([Schaye et al. 2015](#)).

The statistics of galaxy-galaxy lensing systems furthermore allows for a measurement of global cosmological parameters. For example, the lensing statistics of 28 lensed quasars in the Sloan Digital Sky Survey (SDSS) Quasar Lens Search (SQLS) gave an estimate of  $\Omega_{\Lambda} = 0.74 \pm 0.17$ , assuming a spatially flat universe ([Oguri et al. 2012](#)). Selecting lensed sources from bright sub-mm samples is simple and unbiased method because it is based on the source, as the lens is usually faint in the sub-mm. [Eales \(2015\)](#) showed that observations of a sample of 100 lensed *Herschel* sources would be enough to estimate  $\Omega_{\Lambda}$  with a precision of 5 per cent and observations of 1000 lenses would be enough to estimate  $\Omega_{\Lambda}$  with a precision similar to that obtained from the *Planck* observations of the cosmic microwave background.

A high flux density cut-off ( $S_{500\mu\text{m}} > 100\text{mJy}$ ) eliminates a large amount of possible lenses in order to achieve a low contamination rate from unlensed sources ([González-Nuevo et al. 2012](#)). Lowering the cut-off flux density to 80 mJy was already tested in [Wardlow et al. \(2013\)](#). Out of the four galaxies with lensing verification, only one was confirmed to be a lens. In this paper, we will reinvestigate the question of using a lower cut-off flux, by selecting galaxies from the 616.4 sq. deg. H-ATLAS survey. In order to decrease the contamination rate, we impose a photometric cut-off redshift  $z_{\text{phot}} > 2$  based on the *Herschel*-SPIRE fluxes. The probability of lensing below this redshift falls off sharply, because of the smaller volume available between us and the source ([Strandet et al. 2016](#)). We will calculate the expected amount of lensed galaxies in our sample, by comparing the fluxes of our sources to a cosmological evolution model that takes lensing into account.

Our sample selection is based on *Herschel* fluxes, and a known problem of sources selected at 500  $\mu\text{m}$  with *Herschel* is the large solid angle of the beam ([Scudder et al. 2016](#)). This could lead to several sources blending into a single source, and result in a flux that is too large. This is why we observed the majority of our sources at 850  $\mu\text{m}$  with the SCUBA-2 instrument on the James Clerk Maxwell Telescope (JCMT), whose beam has a six times smaller solid angle on the sky. The extra data point should also improve the photometric redshift estimates of our sources.

In Section 2, we discuss the selection of the *Herschel* Bright Sources (HerBS) sample, as well as the observations with SCUBA-2. We describe the results of the JCMT observations in Section 3, where we also remove several blazar contaminants from the sample. We re-derive a spectral template for our sources with spectroscopically determined redshifts in Section 4. We discuss the effects of source confusion, the properties of the template, the redshift distribution of our sample, and estimates of the lensing fraction in Section 5.

Throughout this paper we assume the  $\Lambda$ -CDM model, and the best-fit parameters found by the [Planck Collaboration \(2015\)](#):  $H_0$  67.7 km s<sup>-1</sup> Mpc<sup>-1</sup> and  $\Omega_M = 0.307$ .

## 2 SAMPLE AND MEASUREMENTS

### 2.1 The selection of the HerBS sample

The sample was selected from the brightest, high-redshift sources in the H-ATLAS survey. The H-ATLAS survey used the PACS ([Poglitsch et al. 2010](#)) and SPIRE ([Griffin et al. 2010](#)) instruments on the *Herschel Space Observatory* to observe the North and South Galactic Pole Fields and three equatorial fields to a  $1\sigma$  sensitivity of 5.2 mJy at 250  $\mu$ m to 6.8 mJy at 500  $\mu$ m, although the noise varies per source ([Valiante et al. 2016](#)). The three equatorial fields overlap with the Galaxy And Mass Assembly (GAMA) fields 9, 12 and 15 hours, and from here on we adopt this naming convention for the equatorial fields ([Driver et al. 2011](#); [Liske et al. 2015](#)). The fields are defined in Table 1. In total the H-ATLAS survey detected approximately half a million sources.

We initially selected the HerBS sample from the H-ATLAS point-source catalogues ([Valiante et al. 2016](#)),

The flux densities in the catalogues are not de-boosted, however the flux boosting is negligible compared to the flux uncertainty; around 1 per cent at 80 mJy, and diminishing for increasing flux density, as can be seen in Table 6 of [Valiante et al. \(2016\)](#). We estimated the redshift of each source by fitting a source template to the 250, 350 and 500  $\mu$ m flux densities ([Pearson et al. 2013](#)). We selected the sources at an estimated redshift,  $z_{\text{phot}}$ , greater than 2 and a 500  $\mu$ m flux density,  $S_{500\mu\text{m}}$ , greater than 80 mJy. The source template was a two-temperature modified blackbody from [Pearson et al. \(2013\)](#) (see eq. 3 and Table 5 in our Section 4). This modified blackbody was derived from the *Herschel* PACS and SPIRE flux densities of 40 sources with spectroscopically determined redshifts, with 25 sources at low redshifts ( $z < 1$ ), and only 12 sources at high redshifts ( $z > 2$ ). Our initial sample consisted of the 223 sources.

Where possible we removed sources that are coincident with a large nearby galaxy or a blazar ([Negrello et al. 2010](#); [López-Caniego et al. 2013](#)). However, the preselection of blazars was not complete, and it only became clear after we had carried out the SCUBA-2 observations that we had actually observed several blazars (see Section 3). The final HerBS sample consists of 209 sub-millimetre galaxies after removing all nearby galaxies and blazars, and is listed in Table A1. We plot the positions of the final 209 HerBS sources in the various fields in Figure 1.

Several of the HerBS sources have been investigated individually. [Fu et al. \(2012\)](#) showed that HATLAS J14637.9-001132 (HerBS-2) is a strongly lensed sub-mm galaxy, with a magnification between 7 to 17. [Cox et al. \(2011\)](#) and [Bussmann et al. \(2012\)](#) found that HATLAS J142413.9+022303 (HerBS-13) is a lensed

sub-mm galaxy, with a magnification of 4. At a redshift of 4.24, the source has one of the highest redshifts in our sample. HATLAS J090311.6+003907 (HerBS-19) is also known as SDP.81, and has recently been observed by [ALMA Partnership \(2015\)](#). [Negrello et al. \(2010\)](#) showed SDP.81 is lensed using 880  $\mu$ m Sub-Millimetre Array observations. [Dye et al. \(2015\)](#) and [Tamura et al. \(2015\)](#) reconstructed the galaxy from the ALMA observation, by modelling the distorting effect of the lens. They found a magnification of  $\sim 11$ . This reconstructed image features details on the scale of hundreds of parsecs, and the image shows resolved individual giant molecular clouds in a  $z = 3.04$  galaxy. SDP.81 appears, through reconstructed HST and ALMA imaging, to be two interacting objects, where the dust disk is in a state of collapse.

However, not all our sources are lensed. [Iverson et al. \(2013\)](#) studied HATLAS J084933.4+021442 (HerBS-8), and found it was not a strongly lensed galaxy. Instead, it consists of multiple large galaxies in the process of merging, which has probably triggered starbursts in the individual galaxies, explaining the brightness in sub-mm wavelengths.

Our HerBS sample overlaps partially with the sample from [Negrello et al. \(2017\)](#), as 53 out of the 80 sources in their sample are also found in the HerBS sample. Their sample was designed specifically to find lensed systems, by imposing a flux-density cut-off at 100 mJy at 500  $\mu$ m and did not have a lower redshift limit.

### 2.2 Observations with SCUBA-2

We observed 203 sources with the SCUBA-2 array on the JCMT. The instrument consists of 10,000 Transition Edge Sensor (TES) bolometers, distributed over 4 arrays that observe at 450  $\mu$ m and 4 arrays that observe at 850  $\mu$ m ([Holland et al. 2013](#)). Both wavelengths are observed simultaneously, with the use of a dichroic mirror. The voltage across each array is optimised to ensure as many functional bolometers as possible. The optimised voltage places the majority of the bolometers within their sensitive resistance transition, whereupon any temperature fluctuation causes a current change. The resulting magnetic field variations are read out with separate Superconducting Quantum Interference Devices (SQUIDS) located under each bolometer.

The instrument scans the sky in a DAISY pattern, circling around the source following a continuous petal-like track, providing a central 3 arc-minute region of uniform exposure time, and keeping one part of the array on-source at all times ([Chapin et al. 2013](#)).

The observations conditions were in the grade-3 weather band [ $0.08 < \tau_{1.3\text{mm}} < 0.12$ ], which is only suitable for 850  $\mu$ m observations. The data were flux-calibrated against Uranus, Mars, CRL 618 and CRL 2688 (the Westbrook and Egg Nebulae). The calibrators were observed between 2 and 4 times per observing run, and the flux calibration factors (FCFs) were estimated linearly for observations in between calibrators, and the closest calibrator was used otherwise ([Dempsey et al. 2013](#)).

Our observations consisted of ten-minute exposures for each source. The bolometers are sampled at roughly 200 Hz, and the data is stored in 30-second time slices for each of the arrays, where the first and last time slice of each exposure are flat-fields. Flat-fields probe the responsivity of individual bolometers, and are derived from the bolometer's response to the resistance heaters, which are located next to each bolometer.

**Table 1.** The H-ATLAS fields

Field	Centre		Approximate dimensions		Final surface area [sqr. deg.]	Sources	Surface density [1/sqr. deg]
	RA [hms]	DEC [dms]	RA [deg]	DEC [deg]			
<b>NGP</b>	13:18:00	29:00:00	15	10	<b>170.1</b>	<b>49</b>	<b>0.288</b>
<b>GAMA Total</b>	-	-	-	-	<b>161.6</b>	<b>72</b>	<b>0.446</b>
GAMA 9	09:00:00	00:00:00	12	3	53.43	23	0.430
GAMA 12	12:00:00	00:00:00	12	3	53.56	26	0.485
GAMA 15	14:30:00	00:00:00	12	3	54.56	23	0.422
<b>SGP</b>	23:24:46	-33:00:00	42	6	<b>284.8</b>	<b>88</b>	<b>0.309</b>
<b>Total fields</b>	-	-	-	-	<b>616.4</b>	<b>209</b>	<b>0.339</b>

**Notes:** Reading from the left, the columns are: Column 1 - name of field; Column 2 and 3 - The location of the centre of the field; Column 4 and 5 - The approximate dimensions of the field; Column 6 - The surface area from the final maps (Valiante et al. 2016); Column 7 - The number of final HerBS sources in each field; Column 8 - The surface density of HerBS sources per field.

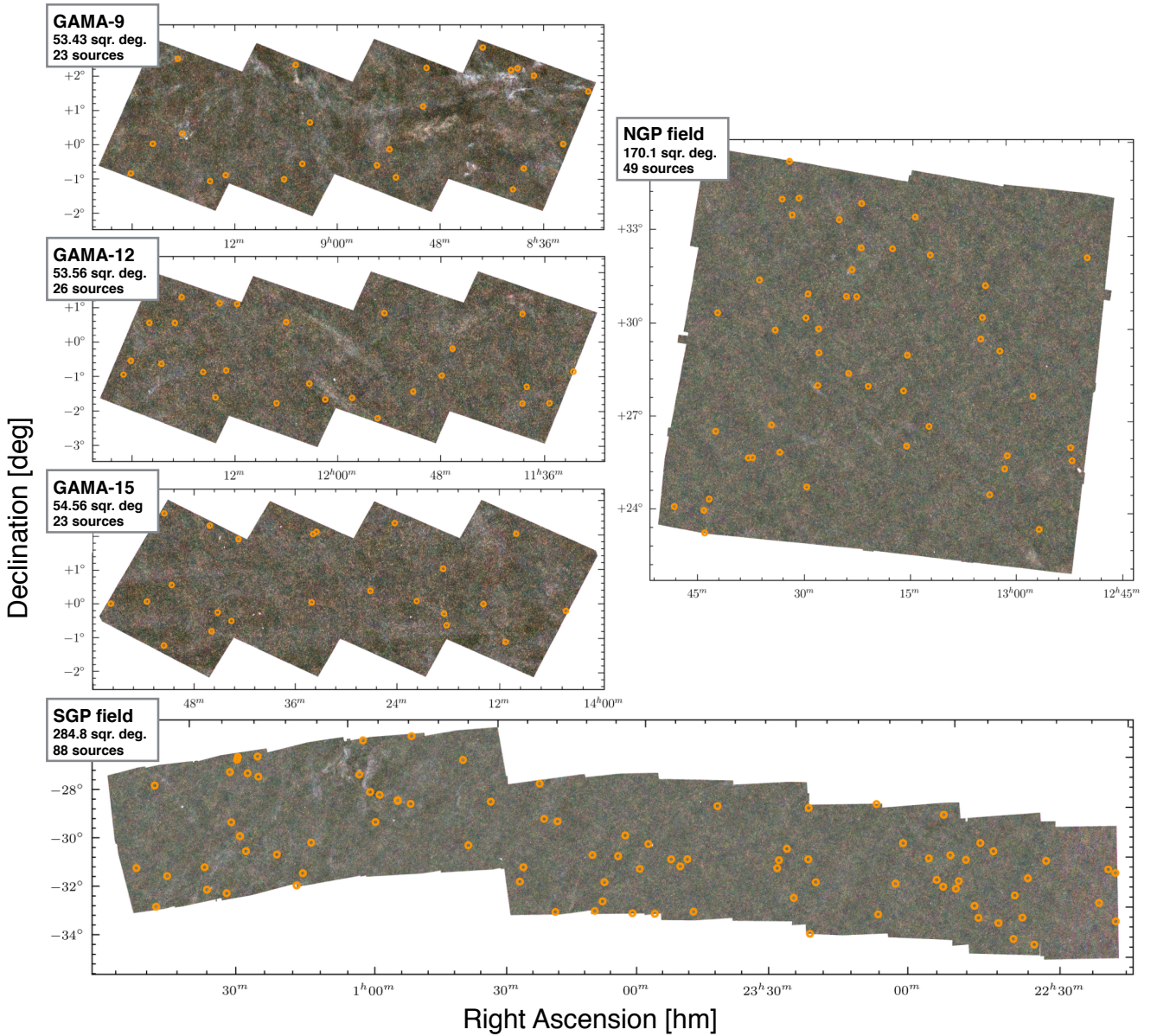


**Figure 1.** *Herschel*/SPIRE color maps of the H-ATLAS fields. The orange circles mark the positions of the 209 HerBS sources. This figure is similar to Figure 2 in (Negrello et al. 2017), and shows how the sources are distributed over the sky.

### 2.3 Data reduction

The entire data reduction method is shown schematically in Figure 2, and is described below. The data reduction was done with the ORAC\_DR pipeline, which uses the KAPPA and SMURF packages from STARLINK, and the PICARD procedures (Thomas et al. 2014).

The basic data consists of the time-dependent signals from each bolometer and information about the specific scanning pattern of the arrays on the sky. The first step of the data reduction method flat-fields and downsamples the data, to correct for individual bolometer performance and to reduce the file size by matching the sampling speed to the spatial scale of the maps. The second step removes the noise components in the signal iteratively, starting with the largest noise component (Chapin et al. 2013). Our final reduced map is achieved with additional data reduction steps: jackknife, fake point-source injection and matched filtering. The final result is a 4 by 4 arcminute image with one arcsecond resolution.

#### The iterative data reduction step (*makemap*)

Sky emission is the dominant noise component, and it is shared by all bolometers. This common-mode signal (COM) is calculated by averaging the signals of all bolometers into one signal per subarray. The common-mode signal is then subtracted from the signal for each bolometer, taking care to adjust for individual bolometer amplification differences (GAI). Bolometers that have a signal that is inconsistent with the common-mode signal are rejected at this stage.

The signal is then corrected for the atmospheric extinction (EXT), a function of precipitable water vapour and telescope pitch, after which a high-pass Fourier filter (FLT) removes low-frequency,  $1/f$  noise. The frequency cut-off is 0.8 Hz, which corresponds to a spatial scale of 200 arc-seconds.

The next step removes the astronomical signal (AST) from the total signal, in order to estimate convergence of our iterative data reduction step. The signals of all bolometers are projected onto the sky, creating an astronomical map of our observation. Many data points contribute to the estimate of the astronomical signal in each spatial pixel, which greatly reduces the noise compared to the time-series data. The map still contains noise, but the assumption made in this step of the iterative data-reduction procedure is that everything in this map is real. The astronomical, space-domain map is then used to create a time-domain signal for each bolometer, by simulating an observation of our astronomical map. This is then removed from the signal for each bolometer.

The time-domain signal for each bolometer should now consist only of noise. This noise is calculated and compared to the convergence criterion (NOI), which is a minimum number of loops (four in this case) and a threshold noise level. If convergence is not reached in the NOI step, all the data-processing steps (FLT, EXT, GAI, COM) are undone, except for the removal of the astronomical signal. This adds back the common-mode noise and the noise removed in the Fourier-filtering step. All the steps (see upper half of Figure 2) are then repeated until the convergence criterion is met. After each cycle the new estimate of the astronomical signal is added to the previous estimate. The final image is obtained when the convergence criterion is met.

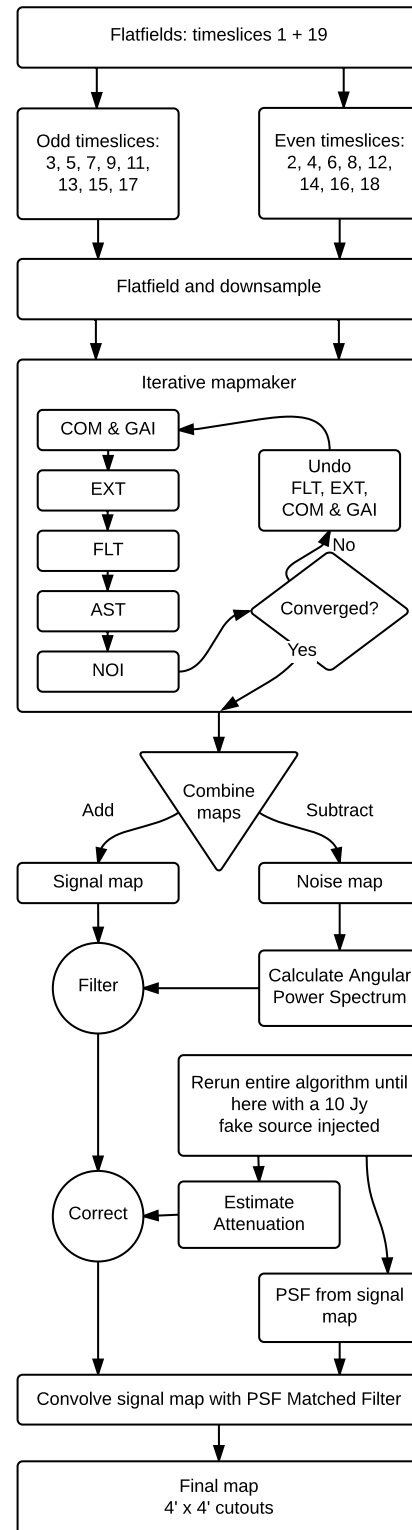


**Figure 2.** This flowchart shows the data reduction steps schematically, starting from the raw data files at the top, working to the reduced cutouts at the bottom. The intricacies are detailed in the data reduction section. For each observation, two sets of timeslices are cleaned and processed through the iterative mapmaker, and these resulting maps are subtracted to provide a jackknife estimate of the noise. A fake source is injected to estimate peak attenuation due to the filtering process, and allows us to create a PSF for the final matched filter step.

*Extra data reduction steps*

Apart from this standard data-reduction procedure, shown in the top half of Figure 2, we added the following additional steps.

For each source, we split the time-slices into two sets. Each set consists of the flat-fields (first and last time slice) and either the odd or even half of the time slices. We ran the iterative mapmaker over each set, separately, which allows us to execute a jackknife step (ORAC\_DR procedure: SCUBA2\_JACKKNIFE).

We used the iterative data reduction step to create a separate map for each half of the data. We subtracted one map from the other to create a noise-map, from which we calculate the angular power spectrum of the noise. We used this angular power spectrum to construct a map-specific Fourier filter. A combined signal map is calculated by adding the two signal maps, and we then applied this Fourier-filter to the signal map.

The high-pass filtering step attenuates the signal, and to account for this, we reran the entire data reduction algorithm with an injected fake source. This fake 10 Jy point-source (FWHM of 13 arc seconds - the main beam size of 850  $\mu\text{m}$  observations with JCMT (Dempsey et al. 2013)) was injected into both the odd and even timeslices, offset at 30 arc seconds from the centre. This extremely bright, fake source allowed us to calculate an effective point spread function (PSF) and also provided an estimate of the signal attenuation due to the high-pass filtering, which usually was around 15 to 20%.

Finally, we applied a matched filter to the signal map, in which we convolved our signal map with the PSF found by injecting a fake source. This provided the final, reduced observation map. We cropped the observation to a 4 by 4 arcminute image, and measured the fluxes by measuring the highest flux density pixel in the central 50 by 50 arcsecond region around the SPIRE-estimated position. We determine a SCUBA-2 detection by a combination of proximity to the *Herschel*-SPIRE 250  $\mu\text{m}$  position and the signal to noise, as shown in Section 3.

**3 RESULTS**

We observed 203 of our preselected H-ATLAS sources with the SCUBA-2 instrument. In the following analysis, we find that fourteen detected sources turn out to be blazars, which leaves our entire HerBS galaxy sample containing 209 sources. 152 of these sources are detected, 27 sources are not detected due to a signal-to-noise cut, and ten sources do have a  $3\text{-}\sigma$  detection, but not within the 10 arcsecond circle around the SPIRE position. These results are summarised in Table 2.

Figure 3 shows the distribution of the maximum signal to noise in a 50 by 50 arcsecond box centered on the SPIRE position, as a function of the position offset.

We decide to define a detected source by a signal-to-noise greater than 3 and a positional offset smaller than 10 arcseconds. Initially, we find 159 sources that satisfy this criterion, 27 sources that are not detected by the signal-to-noise cut, and 17 sources whose positional offset was too large.

For each of the seventeen sources that do not have their maximum flux within the 10 arcsecond circle around the SPIRE position, that do have a signal-to-noise greater than 3, we decreased the size of the searching box to find the peak in flux. Of these seventeen sources, seven sources have fluxes within 10 arc seconds from the SPIRE position with a signal-to-noise greater than 3, as show in boldface in Table 3. These seven sources are added to the detected sources.

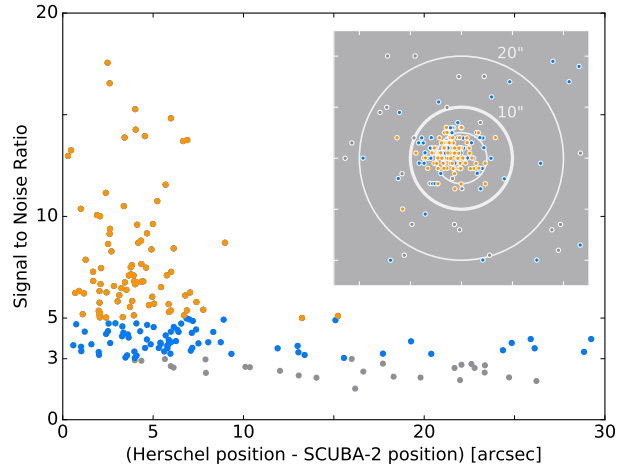


**Figure 3.** The majority of high signal-to-noise SCUBA-2 fluxes lie in a 10 arcsecond circle around the SPIRE position. We choose a cut-off signal-to-noise ratio of  $3\text{-}\sigma$ , and a maximum radius of 10 arcseconds. The fifteen sources with a signal-to-noise ratio between 3 and 5 suggest that the HerBS sources might have two false detections. The overlay graph shows the position of the SCUBA-2 observation, where each point was centered on the SPIRE position.

Of the sources with signal to noise ratios between three and five, fifteen are originally situated outside of the 10 arcsecond circle. These sources are distributed over 89 per cent of the map (the area outside the 10 arcsecond circle). An even distribution of such false detections would result in two ( $\sim 1.7$ ) false detections inside the HerBS catalogue. The overlay graph inside Figure 3 shows a strong correlation for most points around the centre, however all other non-detections appear uniformly scattered, making an even distribution likely.

We know from Negrello et al. (2007) that there is a risk that several of these sources are blazar contaminations. In order to find these contaminants, we plot their flux ratios in Figure 4.

The top panel shows the flux ratios based on just *Herschel* fluxes. We plot  $S_{500\mu\text{m}}/S_{250\mu\text{m}}$  versus  $S_{350\mu\text{m}}/S_{250\mu\text{m}}$ . The sources that lie very close to a known blazar

in the NASA Extragalactic Database (NED) (*black circles*) lie in the same region as the high-redshift HerBS sources (*gray triangles, blue squares and red circles*). We also plot the track for the template we derive in Section 4 through the diagram as the redshift changes (*black line and circles*). Similarly, we show the expected blazar track (assuming synchrotron radiation), for various possible alpha-values (*black dash-dot line and triangles*). Note that both these tracks do not differ significantly from each other. The bottom panel shows the flux ratios of the 203 sources with SCUBA-2 observations. We plot  $S_{850\mu\text{m}}/S_{250\mu\text{m}}$  against  $S_{350\mu\text{m}}/S_{250\mu\text{m}}$ . Most of the galaxies close to a known blazar occupy a different region of the graph, and can be easily identified and removed from the sample.

One of the sources, HerBS-16, does not have the typical flux ratios of a blazar, and has therefore not been removed. The spectrum also looks dust-like, and has consistent photometric redshift estimates, as can be seen in Figure 5. The source, in this case, could be close to the blazar by accident. Only one source close to a known blazar has not been observed, and we have therefore kept it in our HerBS sample (HerBS-112).

The difference between the graphs indicates the need for multi-wavelength observations, in order to reliably remove blazar

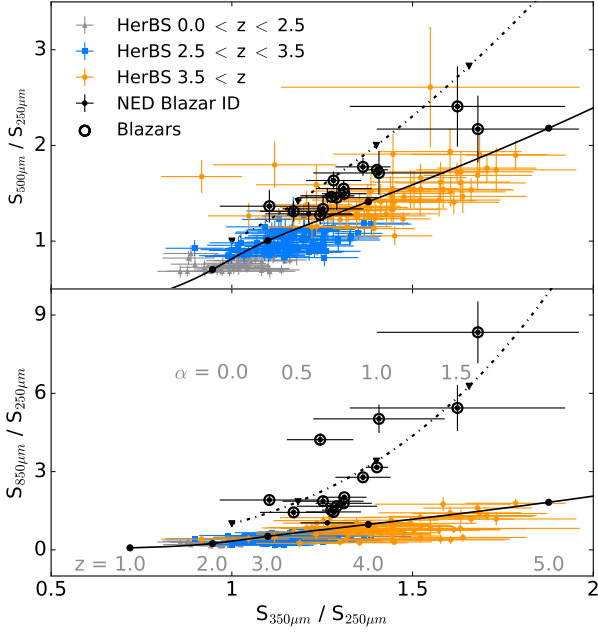


**Figure 4.** The top panel shows the flux ratios based on just *Herschel* fluxes. We plot  $S_{500\mu\text{m}}/S_{250\mu\text{m}}$  versus  $S_{350\mu\text{m}}/S_{250\mu\text{m}}$ . Sources close to a known blazar in NED (black circles) lie in the same region as the high-redshift HerBS sources (gray triangles, blue squares and red circles). The bottom panel shows the flux ratios when we include the SCUBA-2 observations. We plot  $S_{850\mu\text{m}}/S_{250\mu\text{m}}$  against  $S_{350\mu\text{m}}/S_{250\mu\text{m}}$ . Most sources close to a known blazar occupy a different region of the graph, and can be easily identified and removed (black circles). The difference between the graphs indicates the necessity of the 850  $\mu\text{m}$  observations for removing blazar contaminants from the sample. We also plot the track for the template we derive in Section 4 through the diagram as the redshift changes (black line and circles). Similarly, we show the expected blazar track,

contaminants from the sample. We list the *Herschel* SPIRE and SCUBA-2 positions and fluxes of the removed blazars in Table A2.

After removing fourteen blazars from our sample, we are left with 189 HerBS galaxies with SCUBA-2 observations. While some sources close to NED blazars did not have irregular flux ratios, all of the sources with irregular flux ratios are close to known blazars. This suggests our method for finding contaminants in our sample is robust, and thus that the 19 unobserved sources that do not lie close to a NED blazar are not likely to have emission dominated by synchrotron radiation.

For completeness, we plot the blazar spectrum, assuming solely synchrotron radiation, in Figure 4, following equation

$$S_\nu = A \times \nu^{-\alpha}. \quad (1)$$

Here  $S_\nu$  is the flux density at a specific frequency ( $\nu$ ),  $A$  is a constant factor, and  $\alpha$  determines the steepness of the slope in the far-infrared wavelength regime. Most of the blazars lie close to this line. We also calculate the value for  $\alpha$  for each galaxy, by minimizing  $\chi^2$ :

$$\chi^2 = \sum_{i>j} \left[ \frac{(S_i/S_j)_{\text{model}} - (S_i/S_j)_{\text{meas}}}{\sigma_{i,j,\text{meas}}} \right]^2. \quad (2)$$

The index  $i$  and  $j$  iterate over all four wavelengths (250, 350, 500 and 850  $\mu\text{m}$ ), where  $i$ 's wavelength is always larger than  $j$ .  $\sigma_{i,j,\text{meas}}$  is the combined error of  $(S_i/S_j)_{\text{meas}}$ .  $\alpha$ -values range

**Table 2.** SCUBA-2 observations of the HerBS sample

	Sources	Percentage
<b>HerBS galaxies</b>	<b>209</b>	<b>100 %</b>
<b>SCUBA-2 observed</b>	<b>189</b>	<b>90.4 %</b>
Detected ( $> 3\sigma, \theta < 10''$ )	152	69.4 %
Not detected ( $< 3\sigma$ )	27	12.9 %
Not detected ( $> 3\sigma, \theta > 10''$ )	10	8.1 %
<b>Not observed</b>	<b>20</b>	<b>9.6 %</b>
<b>Blazar contaminants</b>	14	

**Table 3.** Re-examined SCUBA-2 observations of HerBS sources with  $\theta > 10$  arc second.

HerBS	$\theta$	S/N	$S_{850\mu\text{m}}$
[–]	["]	[–]	[mJy]
<b>63</b>	<b>9.45</b>	<b>3.19</b>	<b>33.8</b>
<b>75</b>	<b>7.59</b>	<b>4.24</b>	<b>44.9</b>
96	7.84	2.10	19.5
97	6.57	2.49	28.1
<b>101</b>	<b>1.93</b>	<b>3.42</b>	<b>32.5</b>
118	2.28	2.12	23.3
122	6.97	2.43	21.9
131	5.54	2.95	30.3
<b>140</b>	<b>7.14</b>	<b>3.59</b>	<b>30.3</b>
<b>145</b>	<b>9.59</b>	<b>3.17</b>	<b>33.0</b>
146	7.85	2.92	32.1
<b>148</b>	<b>5.40</b>	<b>3.02</b>	<b>29.0</b>
151	6.33	2.34	23.9
163	6.66	1.85	19.1
172	5.92	1.40	13.7
<b>181</b>	<b>4.06</b>	<b>3.81</b>	<b>32.9</b>
195	3.94	2.61	29.5

from 0.24 to 1.66. The individual values can be found in Table A2, and agree well with the positions of the blazar sources in Figure 4.

We provide poststamp cutouts of the observations with SPIRE, SCUBA-2 and fits of our templates (Section 4.1) to the 250, 350, 500 and 850  $\mu\text{m}$  flux densities of each source in Appendix B. Typical cutouts of a source detected by SCUBA-2, a source undetected by SCUBA-2, and a blazar are shown in Figure 5. The bottom row of cutouts shows HerBS-16, which is close to a NED blazar, but has an SED typical of a sub-mm galaxy.

## 4 GALAXY TEMPLATES

We derived a galaxy template for our total sample, by using the subset of HerBS sources that have spectroscopic redshifts. We fitted a two-temperature, modified blackbody spectral energy distribution to the *Herschel* and the SCUBA-2 flux densities of each source. We list the sources with spectroscopic redshifts in Table 4. These spectroscopic redshifts were found by observing sub-mm spectral lines, in order to ensure we are looking at the same source.

This template is necessary to estimate photometric redshifts and luminosities for our entire sample. Similar to the analysis of Pearson et al. (2013), we fitted the template to the SPIRE (250, 350, and 500  $\mu\text{m}$ ) fluxes, and included our JCMT/SCUBA-2 850  $\mu\text{m}$  flux densities. We choose to exclude the PACS photometry of our sources in our analysis, as even the brightest sources are poorly

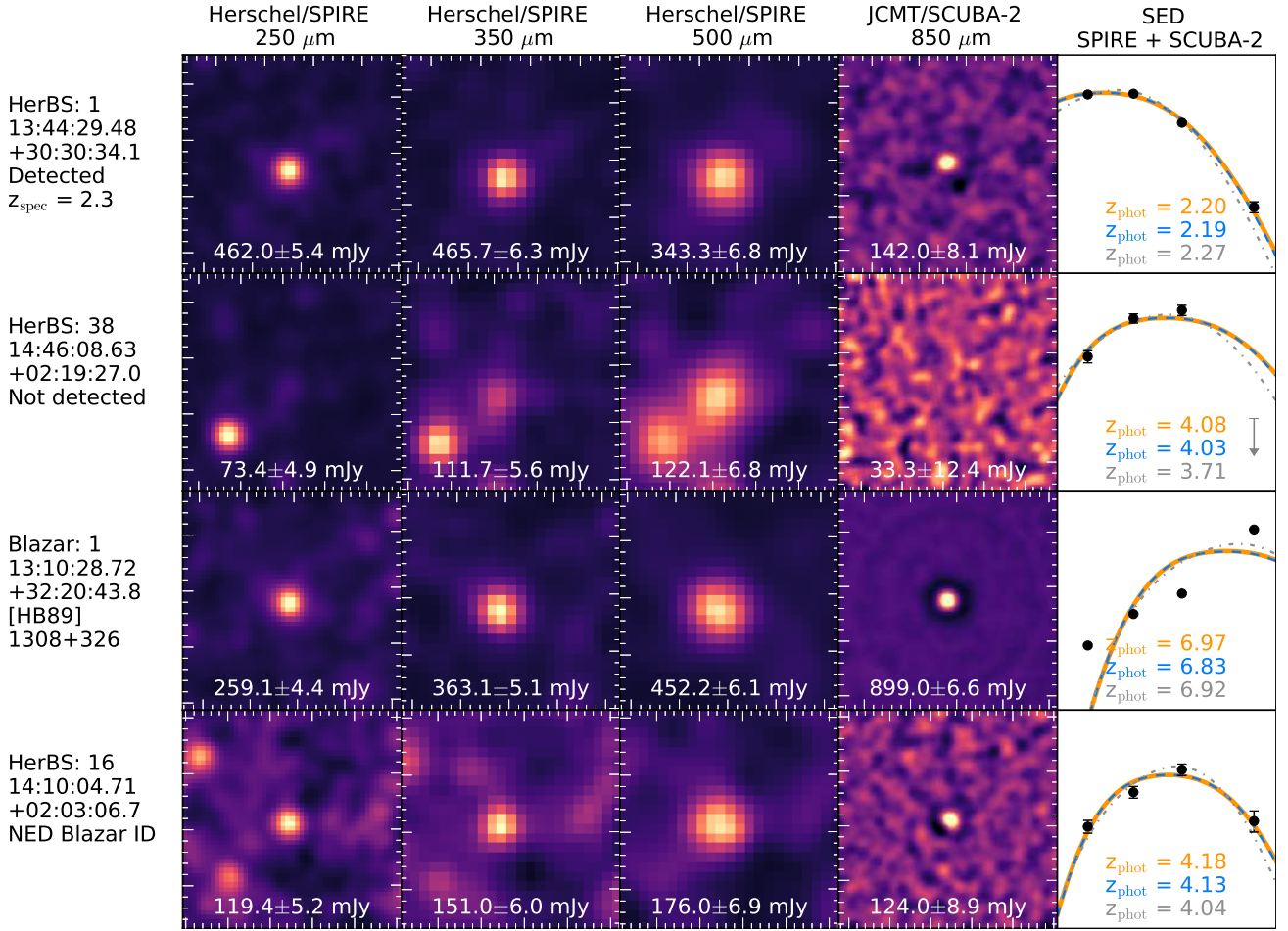


**Figure 5.** This figure shows the four different types of sources we found in the SCUBA-2 850  $\mu\text{m}$  observations of our sample: a galaxy detected with SCUBA-2, a galaxy undetected with SCUBA-2, a blazar, and HerBS-16, which is close to a known blazar, but has an SED typical of thermal emission from dust. The first three columns of cutouts of each source are the *Herschel* observations shown in 4 by 4 arc minute postage stamps. The fourth column shows the 850  $\mu\text{m}$  SCUBA-2 observation in a 4 by 4 arc minute postage stamp.

The final frame is a fitted SED, with the *best-fit* template in orange, *fixed  $\beta$*  template in blue and Pearson's template in grey (Pearson et al. 2013). Similar figures for the entire HerBS sample can be found in Appendix B.

detected, due to the high-redshift limit of our sample. Our spectroscopic sample includes 8 sources used in Pearson's analysis, and 16 new sources, all of which are at high redshifts ( $z_{\text{spec}} > 1.5$ ). We only used HerBS sources for our template to ensure there is 850  $\mu\text{m}$  photometry of our sources, and only used the galaxies with spectroscopic redshifts estimated from more than one line.

#### 4.1 Template fitting

We fitted the template to the sources' flux densities and rest wavelengths, calculated from their spectroscopic redshifts. We assumed a two-temperature modified blackbody template for the SED,

$$S_\nu = A_{\text{off}} \left[ B_\nu(T_h) \nu^\beta + \alpha B_\nu(T_c) \nu^\beta \right], \quad (3)$$

where  $S_\nu$  is the flux at the rest-frame frequency  $\nu$ ,  $A_{\text{off}}$  is the normalisation factor,  $B_\nu$  is the Planck blackbody function,  $\beta$  is the dust emissivity index,  $T_h$  and  $T_c$  are the temperatures of the hot and cold dust components, and  $\alpha$  is the ratio of the mass of the cold to hot dust.

We aimed to minimize the following  $\chi^2$  for the fluxes that

were detected,

$$\chi^2 = \sum_{i=1}^n \chi_i^2 = \sum_{i=1}^n \sum_{j=1}^{\lambda} \left[ \frac{A_i S_{\text{model},i} - S_{\text{meas},i}}{\sigma_{\text{meas},i}} \right]^2, \quad (4)$$

where  $S_{\text{model},i}$  is the predicted flux of the  $i^{\text{th}}$  source (out of  $n$ ) according to equation 3, with the amplitude  $A_{\text{off}}$  set to one.  $S_{\text{meas},i}$  and  $\sigma_{\text{meas},i}$  are the measured signal and noise values. In the case all fluxes of the source were detected, we fitted the amplitude of our template,  $A_i$ , to the rest-wavelength data points analytically in order to decrease computation time,

$$A_i = \left( \sum_{j=1}^{\lambda} \frac{S_{\text{model},j} S_{\text{meas},j}}{\sigma_{\text{meas},j}^2} \right) / \left( \sum_{j=1}^{\lambda} \frac{S_{\text{model},j}^2}{\sigma_{\text{meas},j}^2} \right). \quad (5)$$

Equation 5 is derived by solving  $d\chi_i^2/dA_i = 0$ . We left the

One source with a spectroscopic redshift did not have a detected SCUBA-2 flux, HerBS-71. In this upper-limit case, we calculated the  $\chi^2$  contribution using the method detailed in Sawicki

**Table 4.** The sources from the HerBS sample with measured spectroscopic redshifts.

Robust, multi-line detections					
H-ATLAS name:	HerBS	$z_{\text{spec}}$	$z_{\text{phot}}$	$\Delta z/(1+z)$	Ref.
J083518.4+303034	1	2.30	2.20	0.03	H12
J114637.9-001132	2	3.26	2.80	0.11	H12
J082403.8+334407	3	2.95	3.75	-0.20	H-p
J083051.0+013225	4	3.63	3.09	0.12	R-p
J080520.2+233627	5	3.57	3.72	-0.03	R-p
J082246.8+284449	6	1.68	2.11	-0.16	G13
J082537.0+292326	7	2.78	2.89	-0.03	K-p
J084933.4+021442	8	2.41	2.64	-0.07	L-p
J080214.5+261457	9	3.68	3.87	-0.04	K-p
J113526.2-014606	10	3.13	2.32	0.20	H12
J082620.3+245900	12	3.11	2.29	0.20	R-p
J142413.9+022303	13	4.28	4.53	-0.05	C11
J141351.9-000026	15	2.48	2.62	-0.04	H12
J090311.6+003907	19	3.04	3.76	-0.18	F11
J082310.2+311534	20	1.84	1.88	-0.02	R-p
J083144.0+255054	29	2.34	2.69	-0.11	R-p
J082153.5+341649	30	2.19	3.28	-0.34	R-p
J091840.8+023048	32	2.58	3.03	-0.13	H12
J082949.3+300401	35	2.68	2.73	-0.01	H-p
J091304.9-005344	59	2.63	2.87	-0.07	N10
J115820.1-013752	66	2.19	2.49	-0.09	H-p
J113243.0-005108	71	2.58	3.73	-0.32	R-p
Tentative, single line detections (not used)					
J080532.7+275900	31	2.79	3.25	-0.12	-
J083344.9+000109	88	3.10	3.25	-0.04	-
J113803.6-011737	96	3.15	2.88	-0.07	H12
J113833.3+004909	100	2.22	2.66	-0.14	-

**Notes:** Reading from the left, the columns are: Column 1 - the official H-ATLAS name; Column 2 - HerBS number; Column 3 - spectroscopic redshift; Column 4 - photometric redshift using the *best-fit* model; Column 5 -  $(z_{\text{spec}} - z_{\text{phot}})/(1 + z_{\text{spec}})$ ; Column 6 - Reference for the spectroscopic redshift: N10 = Negrello et al. (2010), F11 = Frayer et al. (2011), H12 = Harris et al. (2012), G13 = George et al. (2013), L13 = Lupu et al. (2012), B13 = Bussmann et al. (2013), H-p = Harris et al. (prep), R-p = Riechers et al. (prep), K-p = Krips et al. (prep), L-p = Lupu et al. (prep).

(2012) and Thomson et al. (2017),

$$\chi^2 = -2 \sum_j \ln \int_{-\infty}^{3\sigma} \exp \left[ -\frac{1}{2} \left( \frac{f - A_j S_{\text{model},j}}{\sigma_{\text{meas},j}} \right)^2 \right] df, \quad (6)$$

where we sum over all non-detections  $j$ , which in our case is only the SCUBA-2 flux of HerBS-71, and integrate the gaussian distribution up to the detection criterion of three times the measured noise ( $3\sigma$ ). The modified  $\chi^2$  statistic quantifies the probability of an event where the noise affected the signal to drop below the detection criterion. In the case the model predicts a flux under the detection limit, there is no discrepancy with the model, and we set the  $\chi^2$ -value to zero.

We did this template fitting for two templates: *best-fit*, where we varied all the parameters ( $T_c$ ,  $T_h$ ,  $\alpha$ , and  $\beta$ ), and *fixed  $\beta$*  where we varied all parameters except  $\beta$ , which we fixed to 2. We also tried keeping  $T_c$ ,  $T_h$ ,  $\alpha$  and  $\beta$  fixed to the values found by Pearson et al. (2013). In this case we found the set of  $A_i$  that gave the minimum  $\chi^2$  fit. The point of this was to determine whether our new templates gave any improvement in the quality of fit over

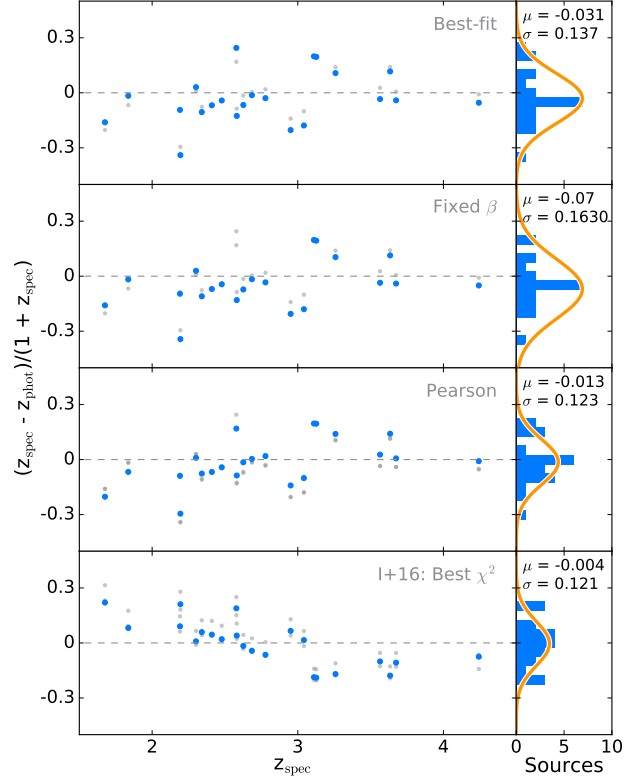


**Figure 6.** The top three panels show  $(z_{\text{spec}} - z_{\text{phot}})/(1 + z_{\text{spec}})$  plotted against the spectroscopic redshift for the three templates. The *blue dots* in each panel show the points for the specified template, while the *smaller grey dots* show the points for the other two templates. The bottom panel shows  $(z_{\text{spec}} - z_{\text{phot}})/(1 + z_{\text{spec}})$  for the three templates used for the redshift estimation in Ivison et al. (2016), where the *blue dots* correspond to the template fit with the lowest  $\chi^2$  for each source individually, and the *smaller grey dots* are the values of the two remaining templates.

that found by Pearson et al. (2013). We estimated the uncertainty on each parameter by incrementally changing this parameter until the minimised  $\chi^2$  changes by of one (one interesting parameter, Avni 1976). The  $\chi^2$  was minimised by allowing the other (two or three) parameters to vary. The best-fit templates are given in Table 4.

## 4.2 Template results

We find a cold- and hot-dust temperature of  $21.29^{+1.35}_{-1.66}$  K and  $45.80^{+2.88}_{-3.48}$  K, a cold-to-hot dust mass ratio of  $26.62^{+5.61}_{-6.74}$  and a  $\beta$  of  $1.83^{+0.14}_{-0.28}$  for the *best-fit* template. The results for the other templates, including the fitting of the templates to redshift and luminosity subsets, can be found in Table 5.

We investigated the usefulness of each template for estimating photometric redshifts, by using each template to estimate the photometric redshift of each source, and then calculating  $(z_{\text{spec}} - z_{\text{phot}})/(1 + z_{\text{spec}})$  for each source. The root mean squared value of  $(z_{\text{spec}} - z_{\text{phot}})/(1 + z_{\text{spec}})$  for the *best-fit* template is 13 %, which is similar to the *fixed- $\beta$*  and Pearson templates. The value of the relative error derived from the *best-fit* template for each source is given in Table 4, and the mean and standard deviations of this quantity for each template are given in Table 5.

Figure 6 shows  $(z_{\text{spec}} - z_{\text{phot}})/(1 + z_{\text{spec}})$  plotted against

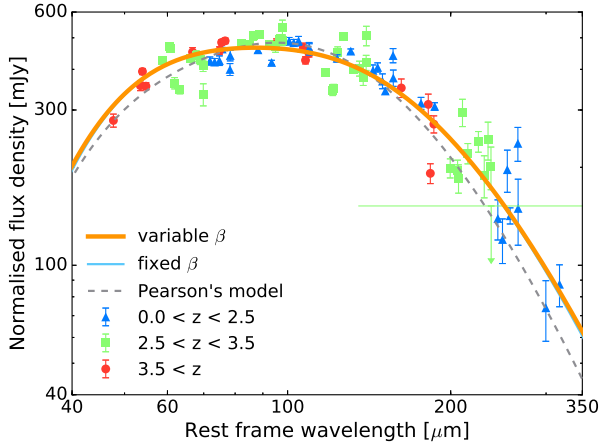


**Figure 7.** The flux densities of the spectroscopic sources plotted against rest-frame wavelength. The curves show the three templates (*best-fit* is the *thick orange line*, *fixed- $\beta$*  is the *thin blue line*, and *Pearson's model* is the *dashed grey line*), and all the flux densities of each source are scaled to produce the same bolometric luminosity as the brightest source (HerBS: 1). The sample is split up in three redshift intervals, to associate each galaxy's four data points more easily.

spectroscopic redshift for the three templates. The three distributions are very similar. We compare the redshift estimates against the method used in [Iverson et al. \(2016\)](#). They fit three different templates (ALESS ([Swinbank et al. 2014](#)), Cosmic Eyelash ([Iverson, R. J. et al. 2010](#); [Swinbank et al. 2010](#)), and the template from [Pope et al. \(2008\)](#)) to the flux measurements, and use the redshift estimate from the spectrum with lowest  $\chi^2$ -value. When we apply this method to our sample of sources with spectroscopic redshifts, we achieve a slightly better redshift accuracy of  $\sim 12\%$ .

We note that the uncertainty in photometric redshift estimation using our new template, obtained from SCUBA-2 and *Herschel* measurements, is not actually any smaller than that using the template that [Pearson et al. \(2013\)](#) obtained from *Herschel* measurements alone. We discuss the significance of this in the Section 5.

Figure 7 shows the normalised flux densities of the spectroscopic sources against their rest-frame wavelength, with the three templates overlaid. The flux-densities are normalised to give each galaxy the same bolometric luminosity as HerBS-1.

We used the photometric redshifts estimates of our *best-fit* template to derive observed bolometric luminosities of the HerBS sources. As the redshift estimates are determined from a different spectrum, some of the photometric redshift estimates,  $z_{\text{phot}}$ , fall below two. They are, however, kept in the HerBS sample, as not to increase the complexity of the selection functions.

We calculate the observed bolometric luminosities by deriving the photometric redshift from our *best-fit* template, and integrating the template from  $\lambda_{\text{rest}} = 8$  to  $1000 \mu\text{m}$ . The estimated redshifts and bolometric luminosities are listed in Table A1, as well as the photometric redshift estimates using the method from [Iverson et al. \(2016\)](#). Figure 8 shows the distribution of sources as a function of redshift and luminosity. This figure shows that the majority of our sources with a spectroscopic redshift are in the higher luminosity range, as typically spectroscopic campaigns aim for the brightest sources first.

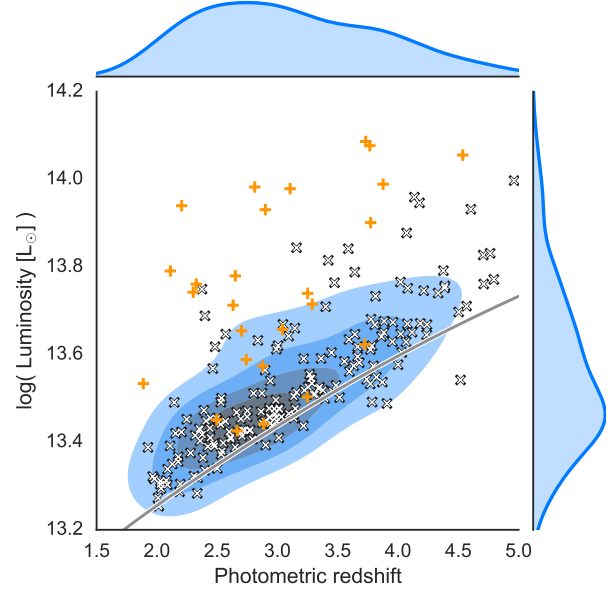


**Figure 8.** Observed bolometric far-infrared luminosity ( $\lambda_{\text{rest}} = 8 - 1000 \mu\text{m}$ ) plotted against photometric redshift, calculated with the *best-fit* template. Sources with spectroscopic redshifts are plotted in *orange pluses*, although the redshifts used in the diagram are their photometric redshifts. The smoothed distributions of redshift and luminosity are shown on the sides of the scatter plots. The grey line shows bolometric luminosity for the *best-fit* template, assuming  $S_{500\mu\text{m}} = 80 \text{ mJy}$ , as a function of redshift.

**Table 5.** The results of the fitting of the total sample, with a variable and fixed beta, and applying the template from [Pearson et al. \(2013\)](#) to our sources.

	Total	Fixed-Beta	Pearson
$T_c$ [K]	$21.29^{+1.35}_{-1.66}$	$20.47^{+0.26}_{-0.26}$	23.9
$T_h$ [K]	$45.80^{+2.88}_{-3.48}$	$44.05^{+0.52}_{-0.55}$	46.9
$\alpha$	$26.69^{+5.61}_{-6.74}$	$30.46^{+1.32}_{-1.42}$	30.1
$\beta$	$1.83^{+0.14}_{-0.28}$	2 (fixed)	2 (fixed)
$\chi^2$	812.58	812.96	1101.03
$\Delta z/(z_{\text{spec}} + 1)$	$-0.03 \pm 0.14$	$-0.03 \pm 0.14$	$-0.01 \pm 0.12$

## 5 DISCUSSION

### 5.1 Source confusion

We have selected our HerBS sample using a  $500 \mu\text{m}$  flux limit. The large beam-width at this wavelength could cause us to confuse multiple line-of-sight sources into a single observed source, and hence yield a  $500 \mu\text{m}$  flux density that is too large.

Observationally, high resolution studies of sub-millimetre galaxies show this to be the case, although the severity of this effect varies from study to study ([Hodge et al. 2013](#); [Koprowski et al. 2014](#)). An SMA study by [Chen et al. \(2013\)](#) of sources selected at  $450 \mu\text{m}$  only found 10 % of the sources to be significantly amplified by line-of-sight sources. An ALMA survey of  $870 \mu\text{m}$  selected ALESS sources finds that up to 50 % of the sources are significantly affected ([Hodge et al. 2013](#); [Karim et al. 2013](#)). Longer wavelengths and higher selection flux densities correlate with more source confusion, although all observational multiplicity studies so far focus on SMGs with a low probability of lensing.

A recent study by Scudder et al. (2016) used Bayesian inference methods to estimate the effects of source confusion in *Herschel* observations at 250  $\mu\text{m}$ . They concluded that individual 250  $\mu\text{m}$  sources are often the combination of emission from more than one galaxy.

The solid angle of the beam of the JCMT at 850  $\mu\text{m}$  is six times smaller than the beam of the 500  $\mu\text{m}$  SPIRE observations. We do not see any of our HerBS sources resolve into multiple  $> 3\sigma$ -detected components. This suggests that our long-wavelength observations are not confused, unless the sources are clustered on a scale smaller than the JCMT's beam size. The small clustering size could be the case, as Karim et al. (2013) finds the multiple emissions are separated less than 6" in the majority of cases of source confusion. Similarly, Chen et al. (2016) measured the clustering of SMGs on scales down to 1.5" using SCUBA-2 combined with deep near-infrared and optical data, and they also report a steep increase in angular correlation below 6". Hayward et al. 2013

A reason for the lack of source confusion could be due to our selection of lensed sources, as the probability for gravitational lensing is small, and two unrelated sources in the same *Herschel* beam are unlikely to be both lensed by the same galaxy.

Strong gravitational lensing could also be caused by a cluster of galaxies, which acts on a longer angular scale. These events are less common (Negrello et al. 2017), however Zavala et al. (2015) did report on the redshifts of cluster-lensed sources, one of which turned out to be three sources that was blended and lensed. We did not exclude these possibilities, however considering their infrequency, we can state that this lensing type would not influence the entire sample.

## 5.2 The diversity of galaxies

In Section 4, we fitted a two-temperature modified blackbody template to 22 HerBS sources with spectroscopic redshifts, the results of which can be seen in Table 5.

Both the fixed- $\beta$  and *best-fit* templates result in similar templates, as the  $\beta$ -value of the *best-fit* template is similar within the error bars. The errors on the *best-fit* template are slightly larger, as more parameters are being fitted. The temperatures on both fitted templates are slightly cooler than the template from Pearson et al. (2013), however we do not find an indication of a cool gas component with a temperature  $T < 20$  K, as found in Planck Collaboration et al. (2011) and Clements et al. (2010). The values we find for the temperatures agree broadly with the initial fitting attempts by Dunne & Eales (2001), and the overall findings of Clements et al. (2010).

The large  $\chi^2$  values in Table 5 imply that a single template is not actually a good representation of the data. We fit our template to 22 galaxies, each with 4 data points, except one source where we only fitted the three SPIRE fluxes, as its SCUBA-2 flux remained undetected. The free parameters in our model are the template parameters (3 or 4) and the amplitudes for each galaxy (22, eq. 5). The expected  $\chi^2$  values for the two models, on the assumption that

they are a good representation of the data, are therefore

$$\begin{aligned}\chi^2_{Best-fit} &\approx N_{\text{data}} - N_{\text{param}} - 1 \\ &\approx 4 \times 22 - 22 - 4 - 1 \\ &\approx 61, \\ \chi^2_{Fixed-\beta} &\approx N_{\text{data}} - N_{\text{param}} - 1 \\ &\approx 4 \times 22 - 22 - 3 - 1 \\ &\approx 62.\end{aligned}$$

However, we observe  $\chi^2$ -values of  $\sim 812$ , indicating that our sources are poorly modelled by a single galaxy template.

We tested the photometric redshift estimates of the templates using the same sources we used to derive the *best-fit* template. However, we found no improvement in accuracy (Table 5) compared to the older template of Pearson et al. (2013). Similarly, Figure 6 shows a similar pattern of redshift errors for all three templates. The redshift estimation by Ivison et al. (2016) might provide a slightly better estimation of the redshift, which are therefore added to the catalogue Table A1. The explanation for this lack of improvement is almost certainly the diversity of the population; the limit on the accuracy of photometric redshift estimates is not set by the accuracy of the average template but by the fact that galaxies have different spectral energy distributions.

## 5.3 Redshift distribution of the HerBS sample

Figure 9 shows the redshift distribution of the HerBS sample, compared against various other galaxy samples, that are summarised in Table 6. The top panel compares the distribution to samples selected with a simple flux cut-off at 500  $\mu\text{m}$ . The sample from Negrello et al. (2017) used a  $S_{500\mu\text{m}} > 100$  mJy flux cut on 600 sq. deg. of the H-ATLAS field (they used a conservative mask on the SGP field). The sample from Nayyeri et al. (2016) used the same flux cut on the 372 sq. deg. HeLMS and HeRS fields. We plot the total sample from Wardlow et al. (2013). They used the 95 sq. deg. HerMES survey, and their 500  $\mu\text{m}$  flux cut-off went down to 80 mJy.

The bottom panel compares the HerBS redshift distribution against samples selected at various wavelengths. The sample from Ivison et al. (2016) is also from the H-ATLAS fields, and contains sources with a color-cut at  $S_{500\mu\text{m}}/S_{250\mu\text{m}} > 1.5$  and  $S_{500\mu\text{m}}/S_{350\mu\text{m}} > 0.85$ , in order to select sources at high redshift. The sources were also selected to have relatively low 500  $\mu\text{m}$  flux density of around 50 mJy, in order to select unlensed sources. Their unlensed nature reduces the uncertainty in the intrinsic luminosity of the source. The South Pole Telescope (SPT) lensed sample was selected from 2500 sq. deg. SPT survey by a flux cut at  $S_{1.4\text{mm}} > 20$  mJy, and demanding the source has a dust-like spectrum. Low-redshift sources were removed with radio and far-infrared flux limits (Weiß et al. 2013; Strandet et al. 2016). The ALESS sample is initially selected from the LESS sample at  $S_{870\mu\text{m}} > 4.4$  mJy from the 0.25 sq. deg. Extended Chandra Deep Field South (ECDFS) field (Weiß et al. 2009). ALMA observations of the LESS sample removed all contaminants, resulting in a final ALMA-LESS (ALESS) sample of 96 SMGs (Simpson et al. 2014).

All samples selected at 500  $\mu\text{m}$  with a simple flux cut have a similar redshift profile, and do not differ significantly from the HerBS sample when we take the photometric redshift cut-off into account. Also, without the photometric redshift cut-off, the standard deviation of the HerBS sample would have been larger.

Typically, higher average redshifts are expected for longer selection wavelengths (Bethemín et al. 2015). We see this for the

SPT sample, which has higher average redshifts. The ALESS sample, selected at  $870\ \mu\text{m}$ , has a higher average redshift than the  $500\ \mu\text{m}$  without redshift constraints, but a lower average redshift than the HerBS sample due to HerBS photometric redshift constraint. The SPT and ALESS samples have a larger standard deviation in their redshifts, because the K-correction is negative for wavelengths between  $850\ \mu\text{m}$  and  $\sim 3\ \text{mm}$ . Comparison with the Ivison sample is difficult because of the more complicated selection criteria they employ.

A way of quantifying the similarity between the samples is using the Kolmogorov-Smirnov test. We compare each sample's sources with a redshift (spectroscopically or photometrically determined) greater than 2 to the photometric redshifts of the HerBS sources with  $z_{\text{phot}} > 2$ . For each sample, we run this method 100,000 times while randomly varying the redshift of each source according to a gaussian distribution with a width of  $\Delta z = 0.15(1 + z)$ . For the comparison to Ivison's sample, we only compare it to HerBS sources with a similar colour cut as they employed ( $S_{500\mu\text{m}}/S_{250\mu\text{m}} > 1.5$  and  $S_{500\mu\text{m}}/S_{350\mu\text{m}} > 0.85$ ), which only 26 HerBS sources follow. For the SPT sample, we used our best-fit template to estimate the flux at  $1.4\text{mm}$ , and only compared the sources that follow the SPT flux cut ( $S_{1.4\text{mm}} > 20\ \text{mJy}$ ), a property only 60 HerBS sources have. The ALESS flux criterion ( $S_{870\mu\text{m}} > 4.4\ \text{mJy}$ ) was also estimated using the best-fit template, and was met by all our 209 sources.

We detail the KS probability values in terms of disagreement between two samples in standard deviations ( $\sigma$ ) in Table 6. A comparison between the redistributed redshifts and the original, unvaried redshift estimates of the HerBS sources gives a  $1.27 \pm 0.45$  times the standard deviation, which indicates we should expect rather large uncertainties in the probability measurements. The spectroscopic redshifts of the HerBS sources disagree with  $2.01 \pm 0.31$  times the standard deviation with the redistributed redshifts. When we compare the photometric redshift estimates of these spectroscopic sources to the HerBS sample, this value drops to  $0.79 \pm 0.56$ . Our HerBS sample thus appears probed evenly by the current set of HerBS sources with spectroscopic redshifts.

The sample from Negrello features more galaxies at low selected redshifts ( $2 < z < 3$ ), causing the disagreement seen by the relatively high KS value. This is contrary to both Nayyeri and Wardlow's samples, who agree strongly with the HerBS sample, suggesting that these sources are drawn from the same population.

## 5.4

[Strandet et al. 2016](#)

10

The SPT also seem to probe similar populations to the HerBS sources, further increasing our suspicion of a high lensing fraction in our sample. A slightly less strong agreement with the ALESS sample was found, which probes deeper on a smaller part of the sky. Interestingly, [Strandet et al. \(2016\)](#) reports a disagreement of around 2.4 standard deviations between the SPT and ALESS sample. The HerBS sample likeness to the SPT sample is larger, sug-

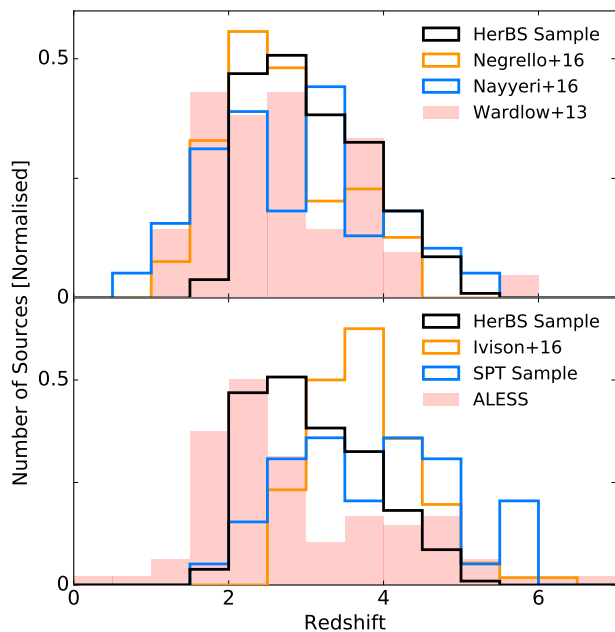


**Figure 9.** The top panel compares the redshift distribution of the HerBS sample (black) to that of three samples selected with *Herschel*/SPIRE at  $500\ \mu\text{m}$ . The bottom panel compares the redshift distribution of the HerBS sample (black) to that of three samples with different selection wavelengths and colour cuts.

gesting this sample is more similar than to the deeper ALESS sample, especially as [Strandet et al. \(2016\)](#) found those two samples to be different. This is further proven by the small lensing fraction in the ALESS sample, compared to the sizeable lensing fraction in the SPT sample, and the lensing fraction we find in Section 5.4. [Hodge et al. 2013](#) [Karim et al. 2013](#)

The low agreement to Ivison's sample suggests that their selection of unlensed SMGs was effective, and it indicates they might select different galaxies than our sample.

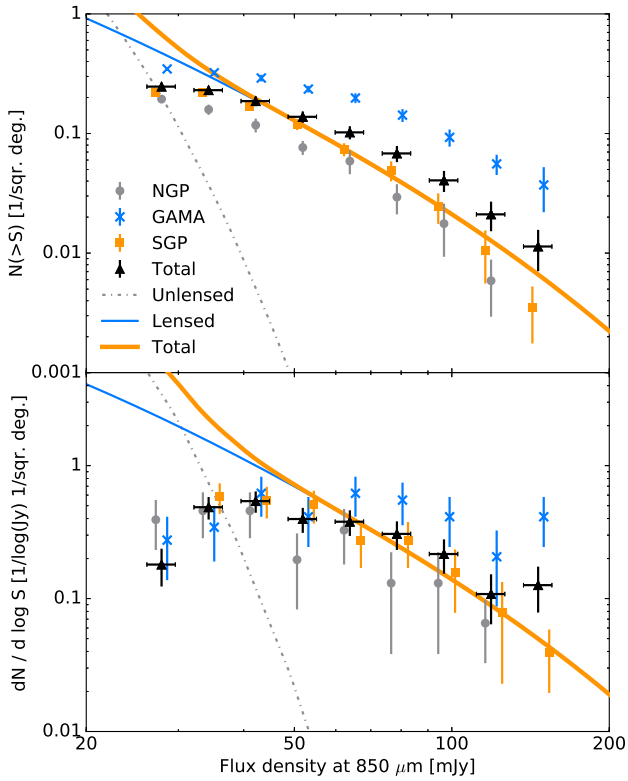
## 5.4 Lensing fraction

The SCUBA-2 observations do not resolve lensing directly, as the beam size ( $13''$ ) is much larger than the typical Einstein rings caused by galaxy-galaxy lensing ( $\sim 1''$ ) ([Bussmann et al. 2013](#); [ALMA Partnership 2015](#)). However, we can estimate the lensing fraction of our sample when we compare the distribution of flux densities of our sources to the predictions of galaxy evolution models that include gravitational lensing.

Here we use the hybrid model by [Cai et al. \(2013\)](#) with a cut-off lensing magnification factor of  $\mu = 30$ . The hybrid model is based on a parametric backward model for redshifts lower than 1.5, whilst it calculates galaxy evolution for redshifts greater than 1.0 using physical models for the evolution of proto-spheroidal galaxies and their associated AGN. The model matches these two approaches to each other in the region between redshift 1.0 and 1.5. We assume all unlensed sources are high-redshift, proto-spheroidal

**Table 6.** Redshift distributions of several sub-mm samples.

Sample	$\langle z \rangle \pm \sigma$	Sources	Surface	KS $\sigma$ -value	Selection criterion
HerBS	$3.09 \pm 0.71$	209	616.4	$1.27 \pm 0.45$	$S_{500\mu\text{m}} > 80$ mJy; $z_{\text{phot}} > 2.0$
HerBS with $z_{\text{spec}}$	$3.07 \pm 0.72$	22	616.4	$2.01 \pm 0.31$	$S_{500\mu\text{m}} > 80$ mJy; $z_{\text{phot}} > 2.0$
Negrello	$2.64 \pm 0.75$	80	616.4	$1.82 \pm 0.77$	$S_{500\mu\text{m}} > 100$ mJy
Nayyeri	$2.77 \pm 1.02$	77	372	$0.66 \pm 0.50$	$S_{500\mu\text{m}} > 100$ mJy
Wardlow	$2.65 \pm 0.90$	42	95	$0.93 \pm 0.66$	$S_{500\mu\text{m}} > 80$ mJy
Iverson	$3.80 \pm 0.67$	112	616.4	$2.31 \pm 0.84$	$S_{500\mu\text{m}} \sim 50$ mJy; $S_{500\mu\text{m}}/S_{250\mu\text{m}} > 1.5$ ; $S_{500\mu\text{m}}/S_{350\mu\text{m}} > 0.85$
SPT sample	$3.81 \pm 1.07$	39	2500	$0.88 \pm 0.55$	$S_{1.4\text{mm}} > 20$ mJy
ALESS	$2.90 \pm 1.22$	96	0.25	$1.26 \pm 0.54$	$S_{870\mu\text{m}} > 4.4$ mJy


**Figure 10.** The top panel shows the cumulative number counts and the bottom panel shows the differential number counts of our HerBS sample, compared to the predictions of the model of Cai et al. (2013) for unlensed (dashed grey line) and lensed (solid blue line) galaxies.

galaxies. We did not observe all of the sample at  $850 \mu\text{m}$ , so we expect that our observed number counts are a lower limit.

Figure 10 shows a comparison of our number counts at  $850 \mu\text{m}$  with the predictions of the model of Cai et al. (2013).

1 We estimate the error on the counts as the square root of the number of sources in each bin. A comparison of our counts with the predicted counts of the unlensed sources (grey dashed line) immediately suggests most of our sources are lensed. We can quantify this as follows.

**Table 7.** Predicted lenses in the HerBS sample

$S_{850\mu\text{m}}$ [mJy]	$N(> S_{850\mu\text{m}})$	Lenses	Percentage
all	$152.0 \pm 0.0$	$128.4 \pm 2.1$	$84.5 \pm 1.4 \%$
30	$133.8 \pm 3.4$	$123.3 \pm 2.9$	$92.2 \pm 0.9 \%$
40	$107.6 \pm 3.9$	$105.2 \pm 3.7$	$97.8 \pm 0.3 \%$
50	$80.8 \pm 3.6$	$80.5 \pm 3.6$	$99.6 \pm 0.1 \%$
60	$60.0 \pm 3.2$	$59.9 \pm 3.2$	$99.9 \pm 0.0 \%$
70	$44.2 \pm 2.9$	$44.2 \pm 2.9$	$100.0 \pm 0.0 \%$
80	$32.4 \pm 2.4$	$32.4 \pm 2.4$	$100.0 \pm 0.0 \%$
90	$23.7 \pm 2.0$	$23.7 \pm 2.0$	$100.0 \pm 0.0 \%$
100	$17.4 \pm 1.7$	$17.4 \pm 1.7$	$100.0 \pm 0.0 \%$
120	$9.5 \pm 1.3$	$9.5 \pm 1.3$	$100.0 \pm 0.0 \%$

Cai et al. 2013

We calculate the total number of lensed sources,

$$N_{\text{lens}}(> S_V) = \sum_i^{N_{\text{gal}}(> S_V)} P_{\text{lens}}(S_{V,i}). \quad (7)$$

We sum the lensing probability,  $P_{\text{lens}}(S_{V,i})$ , over all galaxies brighter than the flux cutoff,  $N_{\text{gal}}(> S_V)$ . We calculate the probability,  $P_{\text{lens}}(S_{V,i})$ , from the relative proportions of the differential number counts predicted for lensed and unlensed galaxies,

$$P_{\text{lens}}(S_{V,i}) = \left[ \frac{dN_{\text{lens}}}{dS_V} \left/ \left( \frac{dN_{\text{proto}}}{dS_V} + \frac{dN_{\text{lens}}}{dS_V} \right) \right]_{S_{V,i}}. \quad (8)$$

The  $N_{\text{lens}}$  term refers to the lensed sources, and the  $N_{\text{proto}}$  term refers to the unlensed proto-spheroidal galaxies. We evaluate the probability at the flux density of the source,  $S_{V,i}$ . Using the bottom panel of Figure 10,  $P_{\text{lens}}$  can be thought of as the fraction lenses (thin blue line) over the total sources (thick orange line).

We iterate this procedure a 1000 times, varying the  $850 \mu\text{m}$  flux with a gaussian distribution with a width of the measurement uncertainty. Table 7 shows the predicted number of lensed sources (eq. 7) and the observed number of sources for all SCUBA-2 detected HerBS sources. All of the errors are the standard deviations. Even for sources at  $S_{850\mu\text{m}} > 30$  mJy, the predicted lensing fraction is  $\sim 92 \%$ , increasing to nearly all sources with  $S_{850\mu\text{m}} > 40$  mJy.

We rerun the same procedure on the  $500 \mu\text{m}$  SPIRE fluxes, which shows that out of all 209 HerBS sources, we expect  $158.1 \pm$

1.7 lensed sources, giving a total lensing fraction of  $75.6 \pm 0.8$  per cent. This suggests that we are missing  $29.7 \pm 1.6$  lensed sources with our SCUBA-2 observations.

Finally we note that our counts in the GAMA fields are systematically higher than those in the other H-ATLAS fields, a point also noticed by [Negrello et al. \(2017\)](#). Using a similar method for the KS-test as described in Subsection 5.3, we calculate the probability for the GAMA and non-GAMA sources, and find a disagreement of  $0.61 \pm 0.47$  standard deviations. This suggests the sources themselves do not differ significantly between the GAMA and the NGP+SGP fields.

## 6 CONCLUSIONS

The HerBS catalogue consists of the brightest, high-redshift sources in the H-ATLAS survey, selected with  $S_{500\mu\text{m}} > 80$  mJy and  $z_{\text{phot}} > 2$ . Initially, we selected 223 sources. SCUBA-2 observations of 203 of these sources allowed us to remove 14 blazars from the HerBS sample, leaving 20 HerBS sources unobserved. 152 out of the 189 confirmed high-redshift galaxies were detected at more than  $3\sigma$ , within 10 arc seconds of the SPIRE position. Currently, our HerBS sample consists of 209 galaxies.

While recent studies like [Scudder et al. \(2016\)](#) suggest a significant effect of source confusion in *Herschel* observations, none of our sources feature spatially-extended emission with  $> 3\sigma$ . While some sources could be confused on a scale not probed by the SCUBA-2 observations, the lack of any signs at the detectable scales gives us little evidence of source confusion significantly affecting the purity of our sample. A reason for this could be due to our high lensing fraction, especially those caused by galaxy-galaxy lensing systems, whose influence is on a smaller angular scale than the less common galaxy-cluster lensing event.

We fitted a two-temperature blackbody as a template to the subset of 22 HerBS sources with spectroscopically determined redshifts, as well as to sub-samples where we divided our sources in redshift or luminosity. We find a cold- and hot-dust temperature of  $21.29^{+1.35}_{-1.66}$  K and  $45.80^{+2.88}_{-3.48}$  K, a cold-to-hot dust mass ratio of  $26.62^{+5.61}_{-6.74}$  and a  $\beta$  of  $1.83^{+0.14}_{-0.28}$ . Overall, the fitted parameters are similar to previous work from [Pearson et al. \(2013\)](#), and they agree broadly with the previous work from [Dunne & Eales \(2001\)](#); [Clements et al. \(2010\)](#). We do not find evidence of any cold gas with temperatures below 20 K, as was found in [Planck Collaboration et al. \(2011\)](#).

We find a high  $\chi^2$  for the template, implying that the spectral energy distributions of the high-redshift population are diverse and cannot be represented by a single template. We showed that our improved template, which incorporates the SCUBA-2 flux densities, does not give a more accurate redshift estimates, which can also be explained by the diversity of the population.

Our sample has a similar redshift distribution as other samples selected at  $500 \mu\text{m}$ , when we take the photometric redshift cut-off into account. Kolmogorov-Smirnov tests indicate that we probe a similar sample of galaxies as the SPT sample.

We calculated the number counts of the  $850 \mu\text{m}$  observations of our sources, and compared them to a galaxy population model by [Cai et al. \(2013\)](#). From this comparison we predict that  $128.4 \pm 2.1$  out of the 152 SCUBA-2 detected, high-redshift galaxies are strongly lensed. A model based around the  $500 \mu\text{m}$  flux suggests a total of  $158.1 \pm 1.7$  of the 209 HerBS sources to be strongly lensed. We report finding more lensed galaxies in the GAMA equatorial

fields, when compared to the galaxy population model of [Cai et al. \(2013\)](#), and the other fields (SGP + NGP).

## ACKNOWLEDGEMENTS

We would like to thank our JCMT operator, James Hoge, for his help at the full-service James Clerk Maxwell Telescope. TB, MS and SAE have received funding from the European Union Seventh Framework Programme ([FP7/2007-2013] [FP&/2007-2011]) under grant agreement No. 607254. The *Herschel*-ATLAS is a project with *Herschel*, which is an ESA space observatory with science instruments provided by European-led Principal Investigator consortia and with important participation from NASA. The *Herschel*-ATLAS website is <http://www.h-atlas.org>. RJI acknowledges support from ERC in the form of the Advanced Investigator Programme, 321302, COSMICISM. LD and SJM acknowledge support from ERC in the form of the Advanced Investigator Programme, 321302, COSMICISM, and the Consolidator Grant CosmicDust (ERC-2014-CoG-647939, PI H.L.Gomez). MJM acknowledges the support of the National Science Centre, Poland through the POLONEZ grant 2015/19/P/ST9/04010. This project has received funding from the European Union's Horizon 2020 research and innovation programme under the Marie Skłodowska-Curie grant agreement No. 665778. MN acknowledges financial support from the European Union's Horizon 2020 research and innovation programme under the Marie Skłodowska-Curie grant agreement No 707601. H.D. acknowledges financial support from the Spanish Ministry of Economy and Competitiveness (MINECO) under the 2014 Ramón y Cajal program MINECO RYC-2014-15686. The authors thank the anonymous referee for his/her comments and suggestions.

## REFERENCES

- ALMA Partnership 2015, *The Astrophysical Journal Letters*, 808, L4  
 Avni Y., 1976, *The Astrophysical Journal*, p. 642  
 Bethermin M., De Breuck, Carlos Sargent, Mark Daddi, Emanuele 2015, *A&A*, 576, L9  
 Blain A. W., Longair M. S., 1993, *Monthly Notices of the Royal Astronomical Society*, 264, 509  
 Blain A. W., Smail I., Ivison R. J., Kneib J. P., Frayer D. T., 2002, *Physics Report*, 369, 111  
 Blain A., Perrotta F., González J. G.-N., Silva L., De Zotti G., Granato G. L., Baccigalupi C., Danese L., 1999, *ApJ*, 512  
 Borys C., et al., 2006, *The Astrophysical Journal*, 636, 134  
 Bussmann R. S., et al., 2012, *The Astrophysical Journal*, 756, 134  
 Bussmann R. S., et al., 2013, *The Astrophysical Journal*, 779, 25  
 Cai Z.-Y., et al., 2013, *The Astrophysical Journal*, 768, 21  
 Casey C. M., Narayanan D., Cooray A., 2014, *Physics Reports*, 541, 45  
 Chapin E. L., Berry D. S., Gibb A. G., Jenness T., Scott D., Tilanus R. P. J., Economou F., Holland W. S., 2013, *Monthly Notices of the Royal Astronomical Society*, 430, 2545  
 Chapman S. C., Perrotta F., González J. G.-N., Silva L., De Zotti G., Granato G. L., Baccigalupi C., Danese L., 2005, *ApJ*, 622  
 Chen C.-C., Cowie L. L., Barger A. J., Casey C. M., Lee N., Sanders D. B., Wang W.-H., Williams J. P., 2013, *The Astrophysical Journal*, 776, 131  
 Chen C.-C., et al., 2016, *The Astrophysical Journal*, 820, 82  
 Clements D. L., Dunne L., Eales S., 2010, *Monthly Notices of the Royal Astronomical Society*, 403, 274  
 Conley A., et al., 2011, *The Astrophysical Journal Letters*, 732, L35  
 Cox P., et al., 2011, *The Astrophysical Journal*, 740, 63  
 Dempsey J. T., et al., 2013, *Monthly Notices of the Royal Astronomical Society*, 430, 2534

- Driver S. P., et al., 2011, *Monthly Notices of the Royal Astronomical Society*, 413, 971
- Dunne L., Eales S. A., 2001, *Monthly Notices of the Royal Astronomical Society*, 327, 697
- Dye S., et al., 2015, *Monthly Notices of the Royal Astronomical Society*, 452, 2258
- Eales S. A., 2015, *Monthly Notices of the Royal Astronomical Society*, 446, 3224
- Eales S., et al., 2010, *Publications of the Astronomical Society of the Pacific*, 122, 499
- Frayser D. T., et al., 2011, *The Astrophysical Journal Letters*, 726, L22
- Fu H., et al., 2012, *The Astrophysical Journal*, 753, 134
- George R. D., et al., 2013, *Monthly Notices of the Royal Astronomical Society: Letters*, 436, L99
- González-Nuevo J., et al., 2012, *The Astrophysical Journal*, 749, 65
- Griffin A., et al., 2010, *A&A*, 518, L3
- Harris A. I., et al., 2012, *The Astrophysical Journal*, 752, 152
- Harris A., Perrotta F., González J. G.-N., Silva L., De Zotti G., Granato G. L., Baccigalupi C., Danese L., in prep.
- Hatsukade B., Tamura Y., Iono D., Matsuda Y., Hayashi M., Oguri M., 2015, *Publications of the Astronomical Society of Japan*, 67, 93
- Hayward C. C., Behroozi P. S., Somerville R. S., Primack J. R., Moreno J., Wechsler R. H., 2013, *Monthly Notices of the Royal Astronomical Society*, 434, 2572
- Hezaveh Y. D., et al., 2016a, *The Astrophysical Journal*, 823, 37
- Hezaveh Y. D., Perrotta F., González J. G.-N., Silva L., De Zotti G., Granato G. L., Baccigalupi C., Danese L., 2016b, *JCAP*11, 048
- Hodge J. A., et al., 2013, *The Astrophysical Journal*, 768, 91
- Holland W. S., et al., 2013, *Monthly Notices of the Royal Astronomical Society*, 430, 2513
- Hughes D. H., et al., 1998, *Nature*, 394, 241
- Ikarashi S., et al., 2011, *Monthly Notices of the Royal Astronomical Society*, 415, 3081
- Iverson R. J. et al., 2010, *A&A*, 518, L35
- Iverson R. J., et al., 2013, *The Astrophysical Journal*, 772, 137
- Iverson R. J., et al., 2016, *The Astrophysical Journal*, 832, 78
- Karim A., et al., 2013, *Monthly Notices of the Royal Astronomical Society*, 432, 2
- Koprowski M. P., Dunlop J. S., Michałowski M. J., Cirasuolo M., Bowler R. A. A., 2014, *Monthly Notices of the Royal Astronomical Society*, 444, 117
- Krips M., Perrotta F., González J. G.-N., Silva L., De Zotti G., Granato G. L., Baccigalupi C., Danese L., in prep., *Monthly Notices of the Royal Astronomical Society*
- Liske J., et al., 2015, *Monthly Notices of the Royal Astronomical Society*, 452, 2087
- López-Cañego M., et al., 2013, *Monthly Notices of the Royal Astronomical Society*, 430, 1566
- Lupu R. E., et al., 2012, *The Astrophysical Journal*, 135, 44
- Lupu R. E., Perrotta F., González J. G.-N., Silva L., De Zotti G., Granato G. L., Baccigalupi C., Danese L., 'in prep.', *Monthly Notices of the Royal Astronomical Society*
- Madau P., Dickinson M., 2014, *Annual Review of Astronomy and Astrophysics*, 52, 415
- Nayeri H., Perrotta F., González J. G.-N., Silva L., De Zotti G., Granato G. L., Baccigalupi C., Danese L., 2016, *ApJ*, 823
- Negrello M., Perrotta F., González J. G.-N., Silva L., De Zotti G., Granato G. L., Baccigalupi C., Danese L., 2007, *Monthly Notices of the Royal Astronomical Society*, 377, 1557
- Negrello M., et al., 2010, *Science (New York, N.Y.)*, 330, 800
- Negrello M., et al., 2017, *Monthly Notices of the Royal Astronomical Society*, 465, 3558
- Oguri M., Perrotta F., González J. G.-N., Silva L., De Zotti G., Granato G. L., Baccigalupi C., Danese L., 2012, *AJ*, 143
- Pearson E. A., et al., 2013, *Monthly Notices of the Royal Astronomical Society*, 435, 2753
- Pilbratt G. L., et al., 2010, *Astronomy and Astrophysics*, 518, L1
- Planck Collaboration 2015, preprint, ([arXiv:1502.01589](https://arxiv.org/abs/1502.01589))
- Planck Collaboration et al., 2011, *A&A*, 536, A16
- Poglitsch et al., 2010, *A&A*, 518, L2
- Pope A., et al., 2008, *The Astrophysical Journal*, 689, 127
- Riechers D., Perrotta F., González J. G.-N., Silva L., De Zotti G., Granato G. L., Baccigalupi C., Danese L., in prep.
- Rybak M., McKean J. P., Vegetti S., Andreani P., White S. D. M., 2015, *Monthly Notices of the Royal Astronomical Society: Letters*, 451, L40
- Sawicki M., 2012, *Publications of the Astronomical Society of the Pacific*, 124, 1208
- Schaye J., et al., 2015, *Monthly Notices of the Royal Astronomical Society*, 446, 521
- Scudder J. M., Oliver S., Hurley P. D., Griffin M., Sargent M. T., Scott D., Wang L., Wardlow J. L., 2016, *Monthly Notices of the Royal Astronomical Society*, 460, 1119
- Simpson J. M., Perrotta F., González J. G.-N., Silva L., De Zotti G., Granato G. L., Baccigalupi C., Danese L., 2014, *ApJ*, 788
- Smail I., Perrotta F., González J. G.-N., Silva L., De Zotti G., Granato G. L., Baccigalupi C., Danese L., 2002, *MNRAS*, 331
- Springel V., et al., 2005, *Nature*, 435, 629
- Strandet M. L., et al., 2016, *The Astrophysical Journal*, 822, 80
- Swinbank A. M., et al., 2010, *Nature*, 464, 733
- Swinbank A. M., et al., 2014, *Monthly Notices of the Royal Astronomical Society*, 438, 1267
- Swinbank A. M., et al., 2015, *The Astrophysical Journal Letters*, 806, L17
- Tamura Y., Oguri M., Iono D., Hatsukade B., Matsuda Y., Hayashi M., 2015, *Publications of the Astronomical Society of Japan*, 67
- Thomas H., Currie M. J., Berry D. S., Parsons H. A., 2014
- Thomson A. P., et al., 2017, *The Astrophysical Journal*, 838, 119
- Treu T., 2010, *Annual Review of Astronomy and Astrophysics*, 48, 87
- Valiante E., et al., 2016, *Monthly Notices of the Royal Astronomical Society*, 462, 3146
- Vegetti S., Lagattuta D. J., McKean J. P., Auger M. W., Fassnacht C. D., Koopmans L. V. E., 2012, *Nature*, 481, 341
- Wardlow J. L., et al., 2011, *Monthly Notices of the Royal Astronomical Society*, 415, 1479
- Wardlow J. L., Perrotta F., González J. G.-N., Silva L., De Zotti G., Granato G. L., Baccigalupi C., Danese L., 2013, *ApJ*, 762
- Weiß A., et al., 2009, *The Astrophysical Journal*, 707, 1201
- Weiß A., et al., 2013, *The Astrophysical Journal*, 767, 88
- Zavala J. A., et al., 2015, *Monthly Notices of the Royal Astronomical Society*, 452, 1140

Table A1: The HerBS sample - SPIRE and SCUBA-2 data. The HerBS number hyperlinks to the NED database at the position of the source. The RA and DEC are the SPIRE-positions,  $\Delta$ RA and  $\Delta$ DEC are the SPIRE positions minus the SCUBA-2 positions. Cursive SCUBA-2 observations are classed as non-detections, as discussed in Section 3. The spectroscopic redshifts are discussed in Section 4,  $z_{\text{phot,temp}}$  refers to the template derived in Section 4, and  $z_{\text{phot}}$  refers to the photometric redshift estimates in Ivison et al. (2016). The bolometric luminosity is calculated using the fitted photometric template

S

No.	H-ATLAS ID	RA [hms]	DEC [dms]	$\Delta$ RA ["]	$\Delta$ DEC ["]	S <sub>250</sub> [mJy]	S <sub>350</sub> [mJy]	S <sub>500</sub> [mJy]	S <sub>850</sub> [mJy]	Z <sub>spec</sub>	Z <sub>phot,temp</sub>	Z <sub>phot,Ivi</sub>	Lum. log(L <sub>⊙</sub> )
<sup>1</sup> 1	J134429.5+303034	206.1228	30.5095	-1.4	2.04	461.9 ± 5.8	465.7 ± 6.5	343.3 ± 7.1	142.0 ± 8.1	2.30	2.21	2.33	13.94
2	J114637.9-001132	176.6582	-0.1923	-3.61	5.15	316.0 ± 6.6	357.9 ± 7.4	291.8 ± 7.7	148.1 ± 10.0	3.26	2.81	2.54	13.98
<sup>1</sup> 3	J132630.1+334408	201.6255	33.7355	-2.11	4.02	190.5 ± 5.6	281.3 ± 5.9	278.6 ± 7.5	121.7 ± 8.7	2.95	3.77	3.21	14.08
<sup>1</sup> 4	J083051.0+013225	127.7127	1.5403	-0.34	4.02	248.5 ± 7.5	305.3 ± 8.1	269.1 ± 8.7	120.9 ± 8.5	3.63	3.10	2.81	13.98
<sup>1</sup> 5	J125632.5+233627	194.1352	23.6076	-1.71	1.98	209.3 ± 5.6	288.5 ± 6.0	264.0 ± 7.0	160.0 ± 9.7	3.56	3.73	3.11	14.09
<sup>1</sup> 6	J132427.0+284450	201.1126	28.7472	-3.17	2.97	342.3 ± 5.6	371.0 ± 5.9	250.9 ± 6.9	71.3 ± 10.5	1.68	2.11	2.27	13.79
<sup>1</sup> 7	J132859.2+292327	202.2468	29.3907	-2.95	5.97	268.4 ± 4.4	296.3 ± 4.8	248.9 ± 5.9	149.1 ± 10.9	2.78	2.90	2.53	13.93
8	J084933.4+021442	132.3893	2.2453	-3.39	-0.95	216.7 ± 7.5	248.5 ± 8.2	208.6 ± 8.6	61.7 ± 9.7	2.41	2.65	2.57	13.78
<sup>1</sup> 9	J125135.3+261458	192.8972	26.2494	0.44	0.01	157.9 ± 5.9	202.2 ± 6.0	206.8 ± 6.9	138.3 ± 10.4	3.68	3.88	3.17	13.99
10	J113526.2-014606	173.8596	-1.7685	-0.01	-0.05	278.8 ± 7.4	282.9 ± 8.2	204.0 ± 8.6	116.3 ± 9.0	3.13	2.33	2.35	13.76
<sup>1</sup> 11	J012407.4-281434	21.0308	-28.2428	-4.57	0.97	257.5 ± 6.4	271.1 ± 6.3	204.0 ± 7.2	94.0 ± 10.3	-	2.37	2.40	13.75
<sup>1</sup> 12	J133008.6+245900	202.5358	24.9833	2.06	0.03	271.2 ± 5.4	278.2 ± 5.9	203.5 ± 6.9	108.0 ± 10.8	3.11	2.30	2.34	13.74
<sup>1</sup> 13	J142413.9+022303	216.0582	2.3842	-3.49	1.97	112.2 ± 7.3	182.2 ± 8.2	193.3 ± 8.5	141.3 ± 9.2	4.24	4.54	3.85	14.06
<sup>1</sup> 14	J013840.5-281856	24.6687	-28.3154	-4.55	-2.01	116.3 ± 6.1	177.0 ± 6.3	179.3 ± 7.5	103.8 ± 10.8	-	4.14	3.35	13.96
<sup>1</sup> 15	J141351.9-000026	213.4666	-0.0075	-2.14	2.97	188.6 ± 7.4	217.0 ± 8.1	176.4 ± 8.7	61.8 ± 8.7	2.48	2.63	2.55	13.71
16	J141004.7+020306	212.5196	2.0519	-2.81	-1.95	119.4 ± 7.3	151.0 ± 8.4	176.0 ± 8.7	123.6 ± 8.9	-	4.18	3.36	13.95
<sup>1</sup> 17	J232531.4-302236	351.3806	-30.3765	-5.33	1.98	175.6 ± 4.7	227.0 ± 5.0	175.7 ± 6.1	100.3 ± 8.7	-	3.16	2.77	13.84
<sup>1</sup> 18	J232419.8-323927	351.0825	-32.6574	-4.59	0.05	212.9 ± 4.7	244.2 ± 5.0	169.4 ± 6.2	72.6 ± 9.7	-	2.40	2.65	13.69
<sup>1</sup> 19	J090311.6+003907	135.7987	0.6521	-0.24	-0.97	133.2 ± 7.4	186.1 ± 8.2	165.2 ± 8.8	108.4 ± 10.4	3.04	3.77	3.11	13.90
<sup>1</sup> 20	J132504.4+311534	201.2682	31.2595	-0.44	4.04	240.6 ± 5.4	226.6 ± 6.0	164.9 ± 7.3	38.8 ± 8.2	1.84	1.89	2.07	13.53
<sup>1</sup> 21	J234418.1-303936	356.0755	-30.6601	-3.05	3.05	125.8 ± 5.5	185.5 ± 5.8	155.1 ± 7.4	80.4 ± 9.1	-	3.59	3.01	13.84
<sup>1</sup> 22	J002624.8-341738	6.6035	-34.2938	-3.21	1.99	137.7 ± 5.6	185.9 ± 6.1	148.8 ± 7.2	91.9 ± 12.8	-	3.42	2.84	13.82
<sup>1</sup> 23	J012046.5-282403	20.1936	-28.401	-5.14	-0.98	103.3 ± 6.1	149.8 ± 6.0	145.7 ± 7.8	100.2 ± 9.3	-	4.07	3.32	13.88
24	J004736.0-272951	11.9	-27.4974	-3.42	-1.98	170.9 ± 5.7	197.1 ± 6.3	145.6 ± 7.4	65.9 ± 9.7	-	2.57	2.53	13.65
<sup>1</sup> 25	J235827.7-323244	359.6153	-32.5456	-3.82	-0.01	112.5 ± 5.0	148.0 ± 5.4	143.4 ± 6.5	72.9 ± 9.6	-	3.64	3.07	13.79
<sup>1</sup> 26	J225844.8-295125	344.6867	-29.8569	-0.03	2.04	175.4 ± 5.6	186.9 ± 6.2	142.6 ± 7.8	70.0 ± 12.2	-	2.48	2.42	13.62
<sup>1</sup> 27	J011424.0-333614	18.6002	-33.6038	-6.66	-1.98	72.2 ± 5.3	129.8 ± 5.6	138.6 ± 7.0	132.5 ± 9.6	-	4.96	4.04	14.00
<sup>1</sup> 28	J230815.6-343801	347.065	-34.6337	1.09	3.98	79.4 ± 5.8	135.4 ± 6.0	140.0 ± 7.4	104.4 ± 10.9	-	4.60	3.81	13.93
<sup>1</sup> 29	J133846.5+255055	204.6939	25.8485	-1.72	2.97	159.0 ± 5.8	183.1 ± 6.0	137.6 ± 7.5	73.5 ± 10.9	2.34	2.70	2.54	13.65

<sup>1</sup> This source is also in Negrello's sample<sup>2</sup> The 850 micron flux of this source was re-evaluated

Table A1: The HerBS sample - SPIRE and SCUBA-2 data. The HerBS number hyperlinks to the NED database at the position of the source. The RA and DEC are the SPIRE-positions,  $\Delta$ RA and  $\Delta$ DEC are the SPIRE positions minus the SCUBA-2 positions. Cursive SCUBA-2 observations are classed as non-detections, as discussed in Section 3. The spectroscopic redshifts are discussed in Section 4,  $z_{\text{phot,temp}}$  refers to the template derived in Section 4, and  $z_{\text{phot,Ivi}}$  refers to the photometric redshift estimates in Ivison et al. (2016). The bolometric luminosity is calculated using the fitted photometric template

No.	H-ATLAS ID	RA [hms]	DEC [dms]	$\Delta$ RA ["]	$\Delta$ DEC ["]	S <sub>250</sub> [mJy]	S <sub>350</sub> [mJy]	S <sub>500</sub> [mJy]	S <sub>850</sub> [mJy]	$z_{\text{spec}}$	$z_{\text{phot,temp}}$	$z_{\text{phot,Ivi}}$	Lum. log(L <sub>⊙</sub> )
<a href="#">30</a>	J132301.7+341649	200.757	34.2804	-3.89	2.98	124.1 ± 5.6	144.5 ± 6.0	137.0 ± 7.2	73.6 ± 8.8	2.19	3.29	2.87	13.72
<sup>1</sup> <a href="#">31</a>	J125652.5+275900	194.2186	27.9834	1.61	1.0	133.9 ± 5.8	164.1 ± 6.0	131.8 ± 7.4	88.6 ± 8.8	2.79	3.25	2.79	13.74
<sup>1</sup> <a href="#">32</a>	J091840.8+023048	139.6702	2.5135	-0.45	2.04	125.7 ± 7.2	150.7 ± 8.2	128.4 ± 8.7	61.5 ± 9.2	2.58	3.04	2.73	13.66
<sup>1</sup> <a href="#">33</a>	J224805.4-335820	342.0223	-33.9723	-1.84	1.05	122.3 ± 6.1	135.6 ± 6.6	126.9 ± 7.5	68.4 ± 9.2	-	3.14	2.74	13.66
<sup>1</sup> <a href="#">34</a>	J133413.8+260458	203.5577	26.0828	-7.14	1.05	136.1 ± 5.4	161.0 ± 5.5	126.5 ± 6.8	61.4 ± 12.6	-	2.84	2.60	13.63
<sup>1</sup> <a href="#">35</a>	J133543.0+300402	203.929	30.0671	-2.74	3.04	136.6 ± 5.4	145.7 ± 5.8	125.0 ± 6.9	58.7 ± 8.7	2.68	2.74	2.53	13.59
<a href="#">36</a>	J235623.1-354119	359.0961	-35.6886	-1.68	4.02	121.5 ± 6.1	161.0 ± 6.7	125.5 ± 7.7	100.1 ± 13.1	-	3.47	2.83	13.76
<sup>1</sup> <a href="#">37</a>	J232623.0-342642	351.596	-34.4451	-0.49	-1.96	153.7 ± 4.8	178.4 ± 5.2	123.5 ± 6.6	57.0 ± 11.3	-	2.46	2.67	13.57
<sup>1</sup> <a href="#">38</a>	J144608.6+021927	221.5359	2.3242	19.42	-12.99	73.4 ± 7.1	111.7 ± 8.1	122.1 ± 8.7	33.3 ± 12.4	-	4.08	3.35	13.75
<sup>1</sup> <a href="#">39</a>	J232900.6-321744	352.2526	-32.2956	-0.7	6.99	118.3 ± 5.1	141.2 ± 5.5	119.7 ± 6.8	52.1 ± 10.6	-	3.00	2.68	13.62
<sup>1</sup> <a href="#">40</a>	J013240.0-330907	23.1666	-33.1518	4.41	2.08	112.0 ± 5.9	148.8 ± 6.5	117.7 ± 7.3	40.7 ± 11.0	-	2.99	2.99	13.61
<a href="#">41</a>	J000124.9-354212	0.3537	-35.7033	2.42	-2.05	63.3 ± 6.2	91.1 ± 6.1	121.7 ± 7.4	56.7 ± 9.3	-	4.39	3.91	13.75
<sup>1</sup> <a href="#">42</a>	J000007.5-334060	0.0312	-33.6833	-2.62	-0.03	130.3 ± 5.8	160.0 ± 6.1	116.2 ± 6.8	84.6 ± 9.0	-	3.05	2.66	13.67
<sup>1</sup> <a href="#">43</a>	J132419.0+320752	201.0792	32.1311	-3.38	2.0	84.4 ± 4.9	116.0 ± 5.2	115.4 ± 6.3	81.2 ± 11.4	-	4.02	3.19	13.77
<sup>1</sup> <a href="#">44</a>	J133255.8+342208	203.2325	34.3689	-1.36	1.99	164.3 ± 5.8	186.8 ± 5.8	114.9 ± 7.2	51.1 ± 10.2	-	2.14	2.54	13.49
<sup>1</sup> <a href="#">45</a>	J005132.8-301848	12.8867	-30.3134	0.12	-5.96	164.6 ± 5.8	160.2 ± 6.1	113.1 ± 7.6	27.3 ± 10.4	-	1.93	2.11	13.39
<sup>1</sup> <a href="#">46</a>	J144556.1-004853	221.4838	-0.8148	3.08	4.99	126.7 ± 7.3	132.6 ± 8.4	111.8 ± 8.7	39.8 ± 10.2	-	2.53	2.52	13.49
<sup>1</sup> <a href="#">47</a>	J225250.7-313658	343.2114	-31.6161	-0.7	4.01	127.4 ± 4.6	138.7 ± 5.1	111.4 ± 6.3	35.5 ± 11.2	-	2.54	2.51	13.50
<a href="#">48</a>	J121301.5-004922	183.2566	-0.8229	-3.14	-0.37	136.6 ± 6.6	142.6 ± 7.4	110.9 ± 7.7	40.7 ± 9.5	-	2.39	2.39	13.47
<sup>1</sup> <a href="#">49</a>	J230546.3-331039	346.4427	-33.1774	-1.87	4.95	76.8 ± 6.0	110.9 ± 6.2	110.4 ± 7.3	40.9 ± 11.6	-	3.78	3.18	13.68
<a href="#">50</a>	J120319.1-011253	180.8296	-1.215	-1.83	3.0	114.3 ± 7.3	142.8 ± 8.2	110.2 ± 8.6	88.8 ± 8.4	-	3.40	2.82	13.71
<a href="#">51</a>	J120709.2-014702	181.7886	-1.7841	-6.67	-0.04	143.2 ± 7.4	149.2 ± 8.1	110.3 ± 8.7	42.5 ± 9.0	-	2.25	2.35	13.45
<sup>1</sup> <a href="#">52</a>	J125125.8+254930	192.8577	25.8249	-2.67	3.0	57.4 ± 5.8	96.8 ± 5.9	109.4 ± 7.2	80.1 ± 12.0	3.44	4.76	3.89	13.83
<a href="#">53</a>	J115112.2-012637	177.801	-1.4437	-3.76	0.16	141.2 ± 7.4	137.7 ± 8.2	108.4 ± 8.8	27.2 ± 8.9	-	2.11	2.33	13.39
<sup>1</sup> <a href="#">54</a>	J131540.6+262322	198.9192	26.3895	-8.92	1.01	94.0 ± 5.7	116.1 ± 6.1	108.6 ± 7.1	96.5 ± 11.1	-	3.81	3.10	13.73
<sup>1</sup> <a href="#">55</a>	J013951.9-321446	24.9664	-32.2462	2.99	5.02	109.0 ± 5.3	116.5 ± 5.5	107.1 ± 6.6	38.2 ± 10.3	-	2.80	2.53	13.51
<sup>1</sup> <a href="#">56</a>	J003207.7-303724	8.0321	-30.6234	-5.82	2.0	80.3 ± 5.4	106.1 ± 5.5	105.8 ± 6.7	47.0 ± 10.3	-	3.64	3.09	13.65
<sup>1</sup> <a href="#">57</a>	J004853.3-303110	12.2219	-30.5193	1.75	-2.06	118.1 ± 4.9	147.3 ± 5.2	105.4 ± 6.4	85.9 ± 10.4	-	3.09	2.65	13.64
<sup>1</sup> <a href="#">58</a>	J130333.1+244643	195.8881	24.7786	-2.63	2.0	99.0 ± 5.5	111.5 ± 5.9	104.5 ± 7.1	59.5 ± 13.0	-	3.22	2.72	13.59
<sup>1</sup> <a href="#">59</a>	J091304.9-005344	138.2708	-0.8956	-2.25	3.02	118.2 ± 6.4	136.8 ± 7.4	104.3 ± 7.7	67.1 ± 9.0	2.63	2.88	2.57	13.57
<a href="#">60</a>	J005724.2-273122	14.351	-27.5229	-7.39	0.03	73.3 ± 5.8	101.2 ± 6.1	103.6 ± 7.5	56.7 ± 9.8	-	3.88	3.21	13.68

<sup>1</sup> This source is also in Negrello's sample

<sup>2</sup> The 850 micron flux of this source was re-evaluated

Table A1: The HerBS sample - SPIRE and SCUBA-2 data. The HerBS number hyperlinks to the NED database at the position of the source. The RA and DEC are the SPIRE-positions,  $\Delta$ RA and  $\Delta$ DEC are the SPIRE positions minus the SCUBA-2 positions. Cursive SCUBA-2 observations are classed as non-detections, as discussed in Section 3. The spectroscopic redshifts are discussed in Section 4,  $z_{\text{phot,temp}}$  refers to the template derived in Section 4, and  $z_{\text{phot,Ivi}}$  refers to the photometric redshift estimates in Ivison et al. (2016). The bolometric luminosity is calculated using the fitted photometric template

No.	H-ATLAS ID	RA [hms]	DEC [dms]	$\Delta$ RA ["]	$\Delta$ DEC ["]	S <sub>250</sub> [mJy]	S <sub>350</sub> [mJy]	S <sub>500</sub> [mJy]	S <sub>850</sub> [mJy]	$z_{\text{spec}}$	$z_{\text{phot,temp}}$	$z_{\text{phot,Ivi}}$	Lum. log(L <sub>⊙</sub> )
<sup>1</sup> 61	J120127.6-014043	180.3652	-1.6789	-1.65	-5.96	67.4 ± 6.5	112.1 ± 7.4	103.9 ± 7.7	79.6 ± 9.4	-	4.38	3.36	13.79
62	J121542.7-005220	183.9281	-0.8723	-1.16	-0.53	119.7 ± 7.4	135.5 ± 8.2	103.4 ± 8.6	36.1 ± 9.6	-	2.44	2.50	13.46
<sup>1</sup> 63	J005132.0-302012	12.8833	-30.3366	-8.09	-4.97	119.3 ± 5.4	121.0 ± 6.0	102.0 ± 7.0	33.8 ± 10.6 <sup>2</sup>	-	2.44	2.41	13.43
<sup>1</sup> 64	J130118.0+253708	195.3252	25.619	-1.62	-2.05	60.2 ± 4.8	101.1 ± 5.3	101.5 ± 6.4	96.5 ± 10.6	4.04	4.71	3.88	13.83
<sup>1</sup> 65	J134422.6+231952	206.0943	23.3311	-0.49	1.95	109.6 ± 6.4	98.3 ± 7.2	101.6 ± 7.7	46.3 ± 7.3	-	2.75	2.53	13.47
66	J115820.1-013752	179.584	-1.6313	-1.67	-1.88	119.8 ± 6.8	123.7 ± 7.7	101.5 ± 7.9	40.2 ± 9.2	2.19	2.50	2.48	13.45
<sup>1</sup> 67	J224207.2-324159	340.5301	-32.6999	-2.19	1.01	73.0 ± 5.9	88.1 ± 6.5	100.8 ± 8.0	61.3 ± 9.8	-	3.88	3.20	13.65
<sup>1</sup> 68	J223753.8-305828	339.4743	-30.9745	-4.33	4.02	139.1 ± 5.3	144.8 ± 5.4	100.5 ± 6.6	48.5 ± 9.1	-	2.20	2.33	13.42
<sup>1</sup> 69	J012416.0-310500	21.0666	-31.0834	-5.03	2.04	140.4 ± 5.8	154.5 ± 6.0	100.3 ± 7.3	41.8 ± 11.2	-	2.16	2.53	13.42
70	J130140.2+292918	195.4176	29.4882	-14.49	20.02	119.6 ± 5.8	136.8 ± 5.8	100.0 ± 7.1	20.2 ± 9.7	-	2.32	2.48	13.42
71	J113243.0-005108	173.1795	-0.8525	-21.18	3.19	67.8 ± 7.3	105.8 ± 8.2	99.8 ± 8.8	25.4 ± 10.0	2.58	3.72	3.25	13.62
72	J144512.1-001510	221.3006	-0.253	-1.38	0.97	78.8 ± 6.5	100.7 ± 7.4	99.6 ± 7.7	68.5 ± 10.0	-	3.81	3.10	13.67
73	J012853.0-332719	22.2208	-33.4554	0.04	6.0	117.1 ± 6.0	129.0 ± 6.2	99.6 ± 7.4	73.3 ± 10.1	-	2.90	2.53	13.56
74	J120600.7+003459	181.5029	0.5832	-0.91	16.21	88.7 ± 7.4	104.1 ± 8.1	98.8 ± 8.7	29.8 ± 9.9	-	2.99	3.03	13.50
75	J011823.8-274404	19.5991	-27.7344	-6.97	2.98	124.4 ± 5.8	134.7 ± 5.9	98.7 ± 7.8	44.9 ± 10.7 <sup>2</sup>	-	2.41	2.42	13.45
76	J133534.1+341835	203.892	34.3097	5.77	-0.0	108.5 ± 5.9	124.3 ± 6.0	98.5 ± 7.0	31.5 ± 8.9	-	2.53	2.53	13.44
77	J005629.6-311206	14.1234	-31.2017	17.72	-14.01	93.2 ± 5.8	135.2 ± 5.9	98.3 ± 7.7	28.6 ± 10.4	-	2.94	2.72	13.54
78	J143352.4+020417	218.4685	2.0715	-4.33	1.03	87.7 ± 7.3	102.4 ± 8.1	98.2 ± 8.8	60.8 ± 8.9	-	3.45	2.90	13.60
79	J131434.1+335219	198.642	33.8719	4.69	-5.03	103.4 ± 5.6	115.3 ± 6.0	97.9 ± 7.3	48.8 ± 9.1	-	2.87	2.62	13.51
80	J230002.6-315005	345.0109	-31.8348	3.68	6.97	122.7 ± 5.7	122.1 ± 6.3	97.7 ± 7.6	22.0 ± 9.5	-	2.18	2.34	13.36
81	J002054.6-312752	5.2274	-31.4646	-7.33	-1.02	82.8 ± 5.6	114.8 ± 5.9	97.5 ± 7.2	42.7 ± 9.6	-	3.36	2.93	13.59
82	J121144.8+010638	182.9369	1.1106	-5.57	-5.04	114.5 ± 6.7	123.2 ± 7.6	96.8 ± 8.0	35.3 ± 9.4	-	2.57	2.53	13.45
83	J121812.8+011841	184.5534	1.3116	-2.73	4.87	49.5 ± 7.2	79.7 ± 8.1	94.1 ± 8.8	71.2 ± 10.0	-	4.79	4.03	13.77
84	J224400.8-340031	341.0035	-34.0086	-7.78	4.01	105.1 ± 5.9	123.0 ± 6.4	97.0 ± 7.6	36.8 ± 9.6	-	2.66	2.57	13.47
85	J114752.7-005831	176.9699	-0.9754	-9.42	3.97	92.1 ± 6.6	104.2 ± 7.4	96.0 ± 7.7	27.2 ± 10.4	-	2.86	2.63	13.47
86	J235324.7-331111	358.3528	-33.1864	-5.37	-0.96	77.4 ± 5.6	90.7 ± 5.8	96.0 ± 7.4	53.0 ± 8.1	-	3.56	3.00	13.58
87	J002533.6-333826	6.3899	-33.6406	-7.5	3.02	114.7 ± 5.2	127.8 ± 6.1	96.0 ± 7.3	30.3 ± 8.0	-	2.36	2.46	13.40
88	J083344.9+000109	128.4374	0.0193	-1.37	-12.98	71.0 ± 7.6	96.0 ± 8.1	95.9 ± 8.8	19.4 ± 8.9	3.10	3.25	3.10	13.50
89	J131611.5+281219	199.0479	28.2053	-2.16	-1.03	71.8 ± 5.7	103.4 ± 5.7	95.7 ± 7.0	81.8 ± 7.3	-	4.21	3.37	13.75
90	J005659.4-295039	14.2473	-29.8441	-1.76	-1.02	59.5 ± 5.9	96.9 ± 6.2	95.6 ± 7.4	48.4 ± 9.2	-	4.08	3.36	13.67
91	J092135.6+000131	140.3987	0.0255	-0.08	1.01	139.2 ± 7.3	128.8 ± 8.1	95.1 ± 8.6	34.0 ± 9.5	-	1.97	2.07	13.32

<sup>1</sup> This source is also in Negrello's sample

<sup>2</sup> The 850 micron flux of this source was re-evaluated

Table A1: The HerBS sample - SPIRE and SCUBA-2 data. The HerBS number hyperlinks to the NED database at the position of the source. The RA and DEC are the SPIRE-positions,  $\Delta$ RA and  $\Delta$ DEC are the SPIRE positions minus the SCUBA-2 positions. Cursive SCUBA-2 observations are classed as non-detections, as discussed in Section 3. The spectroscopic redshifts are discussed in Section 4,  $z_{\text{phot,temp}}$  refers to the template derived in Section 4, and  $z_{\text{phot,Ivi}}$  refers to the photometric redshift estimates in Ivison et al. (2016). The bolometric luminosity is calculated using the fitted photometric template

No.	H-ATLAS ID	RA [hms]	DEC [dms]	$\Delta$ RA ["]	$\Delta$ DEC ["]	S <sub>250</sub> [mJy]	S <sub>350</sub> [mJy]	S <sub>500</sub> [mJy]	S <sub>850</sub> [mJy]	$z_{\text{spec}}$	$z_{\text{phot,temp}}$	$z_{\text{phot,Ivi}}$	Lum. log(L <sub>⊙</sub> )
<a href="#">92</a>	J133808.9+255153	204.5371	25.8647	-	-	42.2 ± 5.7	75.3 ± 6.0	94.9 ± 7.2	-	-	5.23	4.02	13.82
<a href="#">93</a>	J234750.5-352931	356.9606	-35.492	-0.62	0.03	77.3 ± 5.4	87.3 ± 5.7	94.8 ± 7.0	30.2 ± 8.3	-	3.15	2.87	13.48
<a href="#">94</a>	J000950.5-353829	2.4605	-35.6414	4.08	-2.02	100.0 ± 5.4	114.4 ± 6.0	94.7 ± 6.9	33.3 ± 9.4	-	2.70	2.57	13.45
<a href="#">95</a>	J134342.5+263919	205.9272	26.6552	-	-	61.9 ± 5.7	101.3 ± 5.7	94.7 ± 7.6	-	-	4.39	3.48	13.76
<a href="#">96</a>	J113803.6-011737	174.5151	-1.2937	-6.99	-4.28	85.1 ± 7.3	98.4 ± 8.2	94.8 ± 8.8	19.5 ± 9.3 <sup>2</sup>	3.15	2.89	2.72	13.44
<a href="#">97</a>	J224027.8-343135	340.1158	-34.5263	-2.68	6.0	96.1 ± 6.0	98.5 ± 6.3	94.4 ± 7.7	28.1 ± 11.3 <sup>2</sup>	-	2.70	2.78	13.42
<a href="#">98</a>	J001030.1-330622	2.6255	-33.106	-11.67	-3.01	56.3 ± 4.9	51.7 ± 5.0	94.4 ± 6.5	23.4 ± 9.7	-	3.79	4.40	13.49
<a href="#">99</a>	J091809.5+001929	139.5397	0.3248	8.41	-4.04	93.2 ± 7.4	116.6 ± 8.2	94.3 ± 8.7	28.7 ± 8.9	-	2.75	2.67	13.46
<a href="#">100</a>	J113833.3+004909	174.639	0.8194	-0.54	-13.92	96.8 ± 7.3	106.4 ± 8.1	93.4 ± 8.7	21.6 ± 10.4	2.22	2.67	2.53	13.43
<a href="#">101</a>	J011246.5-330611	18.1935	-33.103	-1.94	0.03	118.1 ± 5.8	120.0 ± 6.2	93.9 ± 7.5	32.5 ± 9.5 <sup>2</sup>	-	2.28	2.35	13.38
<a href="#">102</a>	J233024.1-325032	352.6006	-32.8422	-2.92	6.03	74.5 ± 5.7	100.2 ± 6.0	93.7 ± 7.5	52.2 ± 10.2	-	3.67	3.09	13.62
<a href="#">103</a>	J225324.2-323504	343.351	-32.5845	6.64	4.01	126.1 ± 5.3	131.2 ± 5.7	93.5 ± 7.0	59.1 ± 10.9	-	2.36	2.35	13.43
<a href="#">104</a>	J001838.7-354133	4.6613	-35.6925	0.07	5.96	134.0 ± 5.6	128.5 ± 6.1	93.4 ± 6.9	28.2 ± 8.7	-	1.98	2.21	13.32
<a href="#">105</a>	J083932.2-011758	129.8843	-1.2995	-4.69	-5.0	73.8 ± 7.4	88.5 ± 8.1	93.2 ± 8.7	37.6 ± 7.5	-	3.31	2.96	13.51
<a href="#">106</a>	J001802.2-313505	4.509	-31.5847	-1.75	0.94	126.7 ± 5.8	125.6 ± 5.9	93.1 ± 7.4	33.1 ± 9.9	-	2.13	2.33	13.35
<a href="#">107</a>	J014520.0-313835	26.3335	-31.643	4.22	3.94	97.3 ± 6.1	99.1 ± 6.4	93.1 ± 7.8	28.1 ± 7.7	-	2.54	2.53	13.38
<a href="#">108</a>	J083817.4-004134	129.5726	-0.6929	-5.77	1.04	84.5 ± 7.4	106.1 ± 8.2	93.0 ± 8.8	48.4 ± 8.5	-	3.27	2.87	13.56
<a href="#">109</a>	J132900.4+281914	202.2519	28.3206	-	-	121.7 ± 5.4	140.1 ± 5.9	92.8 ± 7.6	-	-	2.35	2.34	13.43
<a href="#">110</a>	J141832.9+010212	214.6375	1.0368	-7.04	0.05	66.0 ± 6.6	106.5 ± 7.5	92.8 ± 7.8	51.8 ± 8.3	-	3.96	3.22	13.67
<a href="#">111</a>	J223942.4-333304	339.9268	-33.5512	23.34	1.04	105.9 ± 6.5	115.6 ± 6.2	92.7 ± 7.4	24.7 ± 10.6	-	2.42	2.70	13.39
<a href="#">112</a>	J133108.4+303034	202.7852	30.5095	-	-	71.8 ± 5.8	87.0 ± 5.8	92.2 ± 7.0	-	-	3.77	3.05	13.61
<a href="#">113</a>	J131211.5+323837	198.0479	32.6436	3.39	-1.95	80.7 ± 5.9	103.4 ± 6.0	92.0 ± 7.0	44.6 ± 8.7	-	3.28	2.89	13.55
<a href="#">114</a>	J012209.5-273824	20.5394	-27.6401	-1.74	-3.99	81.7 ± 5.9	93.8 ± 6.0	91.8 ± 7.7	30.2 ± 10.4	-	2.99	2.73	13.46
<a href="#">115</a>	J133538.3+265742	203.9095	26.9617	-	-	116.2 ± 5.6	133.5 ± 6.0	91.8 ± 6.9	-	-	2.38	2.63	13.42
<a href="#">116</a>	J121348.0+010812	183.4504	1.1368	-2.55	0.49	65.1 ± 7.4	96.6 ± 8.2	93.6 ± 8.5	80.8 ± 9.3	-	4.33	3.38	13.74
<a href="#">117</a>	J000806.8-351205	2.0283	-35.2014	-2.4	3.04	81.0 ± 5.6	112.7 ± 5.9	91.6 ± 6.9	62.7 ± 10.7	-	3.59	2.94	13.63
<a href="#">118</a>	J232200.1-355622	350.5003	-35.9395	0.98	-1.97	60.0 ± 6.3	84.3 ± 6.6	90.9 ± 7.7	23.3 ± 11.1 <sup>2</sup>	-	3.80	3.28	13.57
<a href="#">119</a>	J113833.8-014655	174.6412	-1.7822	-10.21	-12.84	68.5 ± 7.2	85.6 ± 8.1	91.2 ± 8.6	17.4 ± 11.3	-	3.46	2.96	13.52
<a href="#">120</a>	J012222.3-274456	20.593	-27.749	-1.89	3.04	61.8 ± 5.9	101.3 ± 6.4	90.7 ± 7.6	29.5 ± 9.3	-	3.63	3.05	13.57
<a href="#">121</a>	J223615.2-343301	339.0635	-34.5503	-2.9	0.01	85.4 ± 6.0	99.1 ± 6.3	90.6 ± 7.2	54.1 ± 11.4	-	3.28	2.93	13.55
<a href="#">122</a>	J003717.0-323307	9.3208	-32.5519	1.16	5.0	73.7 ± 5.7	95.8 ± 6.0	90.3 ± 7.6	21.9 ± 9.1 <sup>2</sup>	-	3.09	3.16	13.46
<a href="#">123</a>	J233037.3-331218	352.6554	-33.2049	-22.8	-0.01	106.2 ± 5.9	107.9 ± 6.0	90.0 ± 7.5	29.1 ± 11.4	-	2.38	2.39	13.36

<sup>1</sup> This source is also in Negrello's sample

<sup>2</sup> The 850 micron flux of this source was re-evaluated

Table A1: The HerBS sample - SPIRE and SCUBA-2 data. The HerBS number hyperlinks to the NED database at the position of the source. The RA and DEC are the SPIRE-positions,  $\Delta$ RA and  $\Delta$ DEC are the SPIRE positions minus the SCUBA-2 positions. Cursive SCUBA-2 observations are classed as non-detections, as discussed in Section 3. The spectroscopic redshifts are discussed in Section 4,  $z_{\text{phot,temp}}$  refers to the template derived in Section 4, and  $z_{\text{phot,Ivi}}$  refers to the photometric redshift estimates in Ivison et al. (2016). The bolometric luminosity is calculated using the fitted photometric template

No.	H-ATLAS ID	RA [hms]	DEC [dms]	$\Delta$ RA ["]	$\Delta$ DEC ["]	S <sub>250</sub> [mJy]	S <sub>350</sub> [mJy]	S <sub>500</sub> [mJy]	S <sub>850</sub> [mJy]	$z_{\text{spec}}$	$z_{\text{phot,temp}}$	$z_{\text{phot,Ivi}}$	Lum. log(L <sub>⊙</sub> )
<a href="#">124</a>	J122158.5+003326	185.494	0.5573	-3.13	-3.85	135.7 ± 7.3	116.1 ± 8.2	89.8 ± 8.6	42.5 ± 9.3	-	2.03	2.06	13.31
<a href="#">125</a>	J130432.2+295338	196.1341	29.894	-0.15	-2.0	75.7 ± 5.8	103.4 ± 5.7	89.8 ± 7.1	38.9 ± 7.2	-	3.22	2.96	13.52
<a href="#">126</a>	J145135.2-011418	222.8969	-1.2383	1.49	2.05	81.9 ± 7.2	95.9 ± 8.2	89.8 ± 8.8	48.2 ± 10.2	-	3.29	2.95	13.53
<a href="#">127</a>	J132128.6+282020	200.369	28.3389	-	-	110.0 ± 5.5	122.7 ± 6.1	89.5 ± 6.9	-	-	2.44	2.43	13.41
<a href="#">128</a>	J130414.6+303538	196.0607	30.5938	0.74	0.02	106.4 ± 5.7	111.2 ± 5.9	89.2 ± 7.1	37.6 ± 8.0	-	2.47	2.49	13.40
<a href="#">129</a>	J130053.8+260303	195.2242	26.0509	-0.91	-0.02	59.4 ± 5.9	85.4 ± 5.9	89.0 ± 7.0	56.4 ± 8.9	-	4.12	3.35	13.65
<a href="#">130</a>	J142706.4+002258	216.777	0.3829	-6.15	-4.95	119.4 ± 7.3	118.7 ± 8.1	88.8 ± 8.6	24.8 ± 8.4	-	2.03	2.29	13.29
<a href="#">131</a>	J225339.1-325550	343.413	-32.9305	-5.52	-0.01	85.5 ± 5.2	99.7 ± 5.5	88.0 ± 6.9	30.3 ± 10.5 <sup>2</sup>	-	2.88	2.66	13.44
<a href="#">132</a>	J231205.2-295027	348.0216	-29.8407	-2.59	3.08	86.7 ± 5.8	102.6 ± 6.0	90.6 ± 7.8	31.0 ± 10.2	-	2.94	2.71	13.46
<a href="#">133</a>	J134441.5+240345	206.1728	24.0626	-	-	85.4 ± 5.5	98.5 ± 6.1	88.1 ± 7.3	-	-	3.16	2.66	13.51
<a href="#">134</a>	J133440.4+353141	203.6684	35.5281	2.85	-1.0	69.9 ± 5.9	97.3 ± 6.2	87.9 ± 7.3	61.9 ± 10.6	-	3.86	3.16	13.64
<a href="#">135</a>	J225611.7-325653	344.0486	-32.948	-	-	85.4 ± 5.5	96.7 ± 6.2	87.8 ± 7.5	-	-	3.14	2.65	13.50
<a href="#">136</a>	J085308.5-005728	133.2857	-0.9578	-5.61	0.97	68.3 ± 7.5	97.5 ± 8.2	87.7 ± 8.6	50.7 ± 12.2	-	3.78	3.10	13.62
<a href="#">137</a>	J145337.2+000407	223.4052	0.0689	-8.27	-0.96	86.0 ± 7.2	103.6 ± 8.0	87.7 ± 8.6	38.3 ± 8.9	-	2.97	2.72	13.48
<a href="#">138</a>	J011730.3-320719	19.3764	-32.122	-5.53	1.03	120.4 ± 5.8	111.2 ± 6.4	87.4 ± 7.8	32.1 ± 9.6	-	2.09	2.24	13.30
<a href="#">139</a>	J134855.6+240745	207.2317	24.1292	-	-	76.9 ± 5.9	82.9 ± 5.9	87.4 ± 6.8	-	-	3.38	2.77	13.52
<a href="#">140</a>	J142140.3+000447	215.4183	0.08	-5.15	4.96	96.8 ± 7.2	98.5 ± 8.2	87.4 ± 8.7	30.3 ± 8.5 <sup>2</sup>	-	2.53	2.53	13.37
<a href="#">141</a>	J224759.7-310135	341.9986	-31.0264	-11.19	-19.03	122.1 ± 6.1	124.4 ± 6.5	87.3 ± 7.5	28.4 ± 10.5	-	2.03	2.24	13.30
<a href="#">142</a>	J091454.0-010358	138.7253	-1.0663	-2.55	5.05	69.0 ± 7.3	72.2 ± 8.1	87.2 ± 8.5	29.0 ± 9.7	-	3.22	2.96	13.44
<a href="#">143</a>	J141810.0-003747	214.542	-0.6298	-1.26	-0.96	77.7 ± 6.5	97.3 ± 7.4	87.1 ± 7.9	27.6 ± 7.4	-	3.03	2.78	13.46
<a href="#">144</a>	J222629.4-321112	336.6226	-32.1866	3.76	-6.0	98.9 ± 8.4	116.5 ± 8.2	87.0 ± 11.5	32.4 ± 9.5	-	2.48	2.55	13.39
<a href="#">145</a>	J012335.1-314619	20.8963	-31.7718	-3.3	8.95	54.7 ± 6.0	67.4 ± 6.2	86.8 ± 7.7	33.0 ± 10.4 <sup>2</sup>	-	3.87	3.35	13.54
<a href="#">146</a>	J232210.9-333749	350.5454	-33.6304	-7.27	-2.99	122.4 ± 5.2	134.6 ± 5.4	86.6 ± 6.8	32.1 ± 11.1 <sup>2</sup>	-	2.09	2.25	13.34
<a href="#">147</a>	J143403.5+000234	218.5149	0.0429	-2.33	4.04	103.3 ± 7.4	103.3 ± 8.1	86.6 ± 8.5	42.5 ± 9.1	-	2.55	2.42	13.40
<a href="#">148</a>	J224026.5-315155	340.1106	-31.8652	-5.29	-0.97	120.6 ± 5.0	121.2 ± 5.5	86.3 ± 6.8	29.0 ± 9.6 <sup>2</sup>	-	2.08	2.24	13.31
<a href="#">149</a>	J133827.6+313956	204.6149	31.6654	-3.83	1.0	101.5 ± 5.5	103.3 ± 6.0	86.0 ± 7.0	26.0 ± 8.9	-	2.31	2.40	13.32
<a href="#">150</a>	J122459.1-005647	186.2466	-0.9465	-2.84	-6.19	53.6 ± 7.2	81.3 ± 8.3	92.0 ± 8.9	64.0 ± 10.5	-	4.57	3.54	13.71
<a href="#">151</a>	J012530.5-302509	21.3772	-30.4192	6.26	-1.0	64.2 ± 5.8	92.9 ± 5.8	85.8 ± 6.9	23.9 ± 10.2 <sup>2</sup>	-	3.49	3.08	13.53
<a href="#">152</a>	J133057.5+311734	202.7394	31.2928	-2.85	9.98	47.7 ± 5.6	53.4 ± 6.0	85.8 ± 6.9	23.3 ± 9.0	-	3.91	4.05	13.49
<a href="#">153</a>	J144243.4+015504	220.6809	1.9179	1.22	0.04	123.2 ± 7.2	133.4 ± 8.1	85.7 ± 8.8	44.5 ± 10.3	-	2.18	2.51	13.37
<a href="#">154</a>	J132258.2+325050	200.7423	32.8473	-0.68	0.0	79.1 ± 5.6	87.9 ± 5.9	85.6 ± 7.2	52.1 ± 8.4	-	3.35	3.04	13.53
<a href="#">155</a>	J000330.7-321136	0.8778	-32.1934	3.1	-2.97	59.9 ± 5.8	94.2 ± 5.8	85.6 ± 7.2	46.0 ± 10.6	-	3.95	3.22	13.63

Table A1: The HerBS sample - SPIRE and SCUBA-2 data. The HerBS number hyperlinks to the NED database at the position of the source. The RA and DEC are the SPIRE-positions,  $\Delta$ RA and  $\Delta$ DEC are the SPIRE positions minus the SCUBA-2 positions. Cursive SCUBA-2 observations are classed as non-detections, as discussed in Section 3. The spectroscopic redshifts are discussed in Section 4,  $z_{\text{phot,temp}}$  refers to the template derived in Section 4, and  $z_{\text{phot,Ivi}}$  refers to the photometric redshift estimates in Ivison et al. (2016). The bolometric luminosity is calculated using the fitted photometric template

No.	H-ATLAS ID	RA [hms]	DEC [dms]	$\Delta$ RA ["]	$\Delta$ DEC ["]	S <sub>250</sub> [mJy]	S <sub>350</sub> [mJy]	S <sub>500</sub> [mJy]	S <sub>850</sub> [mJy]	$z_{\text{spec}}$	$z_{\text{phot,temp}}$	$z_{\text{phot,Ivi}}$	Lum. log(L <sub>⊙</sub> )
<a href="#">156</a>	J002144.8-295218	5.4368	-29.8716	0.35	3.97	103.7 ± 5.7	91.3 ± 6.1	85.4 ± 6.9	35.0 ± 10.4	-	2.40	2.34	13.34
<a href="#">157</a>	J084957.7+010713	132.4905	1.1204	-4.84	-1.03	81.2 ± 7.3	98.9 ± 8.2	85.2 ± 8.7	49.3 ± 8.2	-	3.25	2.83	13.53
<a href="#">158</a>	J132329.9+311528	200.8745	31.2579	-0.17	-2.03	64.7 ± 5.4	75.7 ± 6.2	85.1 ± 7.2	39.5 ± 7.7	-	3.52	3.11	13.50
<a href="#">159</a>	J235122.0-332902	357.8416	-33.4839	-0.12	5.99	92.1 ± 5.9	98.3 ± 5.9	85.0 ± 7.1	40.5 ± 10.6	-	2.77	2.53	13.43
<a href="#">160</a>	J011014.5-314814	17.5604	-31.8038	-0.06	-5.01	48.6 ± 5.6	84.2 ± 6.0	84.8 ± 7.1	57.6 ± 10.1	-	4.50	3.53	13.70
<a href="#">161</a>	J122407.4-003247	186.031	-0.5465	1.1	-1.12	56.5 ± 7.3	75.7 ± 8.1	82.4 ± 8.8	32.7 ± 9.7	-	3.82	3.24	13.55
<a href="#">162</a>	J144334.3-003034	220.893	-0.5095	-1.81	6.0	76.1 ± 6.5	92.5 ± 7.3	84.6 ± 7.7	42.7 ± 11.0	-	3.34	2.81	13.52
<a href="#">163</a>	J000745.8-342014	1.941	-34.3373	2.99	-5.96	92.7 ± 5.9	92.6 ± 5.9	84.5 ± 7.6	<i>19.1 ± 10.3<sup>2</sup></i>	-	2.50	2.43	13.34
<a href="#">164</a>	J121416.3-013704	183.5682	-1.6179	-4.33	0.7	88.0 ± 6.4	99.3 ± 7.4	84.3 ± 7.7	39.6 ± 10.0	-	2.98	2.64	13.46
<a href="#">165</a>	J090613.8-010042	136.5576	-1.0118	-14.64	9.98	73.4 ± 7.4	80.2 ± 8.0	84.3 ± 8.7	<i>26.7 ± 9.7</i>	-	3.01	2.73	13.41
<a href="#">166</a>	J222503.8-304848	336.2657	-30.8133	-1.5	5.97	32.4 ± 7.2	50.1 ± 8.5	84.3 ± 10.3	<i>26.7 ± 10.4</i>	-	4.52	4.91	13.54
<a href="#">167</a>	J130341.5+313754	195.9229	31.6315	4.51	16.01	52.1 ± 5.6	82.2 ± 6.0	84.3 ± 7.2	<i>21.5 ± 9.1</i>	-	3.77	3.34	13.53
<a href="#">168</a>	J225045.5-304719	342.6896	-30.7887	1.13	3.04	65.5 ± 6.1	88.1 ± 6.1	84.0 ± 7.5	68.9 ± 10.6	-	4.02	3.19	13.65
<a href="#">169</a>	J083859.3+021325	129.7472	2.2239	3.33	4.97	95.2 ± 7.5	105.2 ± 8.2	84.0 ± 8.7	42.3 ± 7.9	-	2.71	2.53	13.43
<a href="#">170</a>	J000455.4-330812	1.2307	-33.1366	0.81	-1.0	61.9 ± 5.4	78.8 ± 6.0	83.8 ± 7.0	76.4 ± 9.7	-	4.24	3.35	13.67
<a href="#">171</a>	J083945.0+021021	129.9378	2.1728	-	-	71.3 ± 7.3	97.4 ± 8.1	83.4 ± 8.6	-	-	3.66	2.88	13.60
<a href="#">172</a>	J145040.5+003333	222.6688	0.5594	5.1	-3.0	76.1 ± 7.4	85.1 ± 8.1	83.3 ± 8.9	<i>13.7 ± 9.6<sup>2</sup></i>	-	2.90	2.72	13.39
<a href="#">173</a>	J131804.7+325016	199.5195	32.8379	-5.11	-4.99	73.3 ± 5.6	92.7 ± 6.0	83.3 ± 7.2	31.7 ± 9.0	-	3.14	2.83	13.46
<a href="#">174</a>	J003728.7-284125	9.3696	-28.6903	-15.94	8.96	95.6 ± 5.7	84.8 ± 5.9	83.2 ± 7.4	<i>19.6 ± 9.3</i>	-	2.33	2.51	13.28
<a href="#">175</a>	J121900.8+003326	184.7537	0.5575	-0.63	-0.93	56.7 ± 7.4	81.5 ± 8.0	81.9 ± 8.8	54.8 ± 10.5	-	4.24	3.36	13.65
<a href="#">176</a>	J131222.2+270219	198.0926	27.0386	-	-	76.7 ± 5.5	90.1 ± 5.8	82.9 ± 6.9	-	-	3.30	2.72	13.51
<a href="#">177</a>	J115433.6+005042	178.6402	0.8451	1.79	2.0	53.9 ± 7.4	85.8 ± 8.1	83.9 ± 8.6	94.4 ± 10.9	-	4.71	3.89	13.76
<a href="#">178</a>	J011850.1-283642	19.7087	-28.6118	-3.51	1.06	93.3 ± 5.9	113.2 ± 6.1	82.7 ± 7.4	34.9 ± 8.6	-	2.61	2.58	13.41
<a href="#">179</a>	J115521.0-021329	178.8376	-2.2249	-1.16	1.33	62.9 ± 7.3	79.9 ± 8.2	82.2 ± 8.5	70.2 ± 11.3	-	4.07	3.19	13.63
<a href="#">180</a>	J131539.2+292219	198.9134	29.372	-2.16	5.97	88.2 ± 5.4	102.6 ± 5.8	82.6 ± 7.1	31.7 ± 7.2	-	2.65	2.58	13.39
<a href="#">181</a>	J005850.0-290122	14.7082	-29.0229	-0.61	-4.02	92.5 ± 5.7	116.6 ± 6.0	82.6 ± 7.2	32.9 ± 8.8 <sup>2</sup>	-	2.61	2.81	13.41
<a href="#">182</a>	J230538.5-312204	346.4106	-31.3678	-	-	89.0 ± 5.7	109.1 ± 6.2	82.3 ± 7.9	-	-	2.93	2.59	13.48
<a href="#">183</a>	J090453.2+022017	136.222	2.3383	-1.34	-3.03	87.0 ± 7.2	98.2 ± 8.0	82.3 ± 8.8	44.5 ± 8.8	-	2.94	2.64	13.46
<a href="#">184</a>	J234955.7-330833	357.4821	-33.1425	-	-	91.9 ± 5.9	107.6 ± 6.0	82.3 ± 7.1	-	-	2.73	2.54	13.43
<a href="#">185</a>	J092408.8-005017	141.0368	-0.8382	-2.64	1.03	71.8 ± 7.4	87.7 ± 8.2	82.2 ± 8.5	61.6 ± 9.4	-	3.68	3.08	13.58
<a href="#">186</a>	J013217.0-320953	23.0708	-32.1647	-8.36	3.0	57.5 ± 5.4	79.2 ± 5.9	82.2 ± 7.0	51.3 ± 10.4	-	4.03	3.25	13.60

<sup>1</sup> This source is also in Negrello's sample

<sup>2</sup> The 850 micron flux of this source was re-evaluated

Table A1: The HerBS sample - SPIRE and SCUBA-2 data. The HerBS number hyperlinks to the NED database at the position of the source. The RA and DEC are the SPIRE-positions,  $\Delta$ RA and  $\Delta$ DEC are the SPIRE positions minus the SCUBA-2 positions. Cursive SCUBA-2 observations are classed as non-detections, as discussed in Section 3. The spectroscopic redshifts are discussed in Section 4,  $z_{\text{phot,temp}}$  refers to the template derived in Section 4, and  $z_{\text{phot,Ivi}}$  refers to the photometric redshift estimates in Ivison et al. (2016). The bolometric luminosity is calculated using the fitted photometric template

No.	H-ATLAS ID	RA [hms]	DEC [dms]	$\Delta$ RA ["]	$\Delta$ DEC ["]	S <sub>250</sub> [mJy]	S <sub>350</sub> [mJy]	S <sub>500</sub> [mJy]	S <sub>850</sub> [mJy]	$z_{\text{spec}}$	$z_{\text{phot,temp}}$	$z_{\text{phot,Ivi}}$	Lum. log(L <sub>⊙</sub> )
<a href="#">187</a>	J083705.2+020033	129.2719	2.0092	2.4	0.02	108.0 ± 7.2	97.0 ± 8.1	82.0 ± 8.6	31.3 ± 7.4	-	2.19	2.24	13.29
<a href="#">188</a>	J084259.9+024959	130.7498	2.8331	-	-	84.2 ± 7.4	101.5 ± 8.1	81.8 ± 8.6	-	-	3.02	2.63	13.48
<a href="#">189</a>	J225600.7-313232	344.0029	-31.5421	-1.36	0.99	119.5 ± 5.9	132.1 ± 6.2	81.7 ± 7.6	74.2 ± 10.2	-	2.50	2.58	13.45
<a href="#">190</a>	J090405.3-003332	136.0222	-0.5591	-0.5	0.99	82.7 ± 7.3	90.8 ± 8.2	81.6 ± 8.7	42.3 ± 8.2	-	3.00	2.69	13.45
<a href="#">191</a>	J124753.3+322448	191.9722	32.4134	-3.12	0.97	57.7 ± 5.9	81.5 ± 5.8	81.5 ± 7.5	37.8 ± 9.2	-	3.74	3.19	13.54
<a href="#">192</a>	J222628.8-304421	336.6202	-30.739	-	-	101.3 ± 7.7	97.0 ± 8.3	81.5 ± 9.9	-	-	2.34	2.33	13.32
<a href="#">193</a>	J085352.0-000804	133.4669	-0.1346	-3.58	-0.99	96.0 ± 7.3	95.0 ± 8.1	81.4 ± 8.9	52.9 ± 9.5	-	2.77	2.53	13.43
<a href="#">194</a>	J085521.1-003603	133.8382	-0.6011	4.66	-0.99	95.6 ± 7.5	98.8 ± 8.1	81.3 ± 8.5	45.8 ± 8.1	-	2.71	2.53	13.41
<a href="#">195</a>	J145754.2+000018	224.476	0.0051	3.61	4.02	70.3 ± 7.3	92.7 ± 8.1	81.0 ± 8.8	29.5 ± 10.0 <sup>2</sup>	-	3.14	2.85	13.45
<a href="#">196</a>	J134403.1+242628	206.0131	24.4411	-	-	86.9 ± 5.7	92.3 ± 6.3	81.0 ± 7.1	-	-	2.79	2.53	13.41
<a href="#">197</a>	J122034.2-003805	185.1429	-0.635	11.49	13.92	81.9 ± 7.5	93.8 ± 8.2	84.8 ± 8.7	37.7 ± 11.6	-	2.96	2.65	13.44
<a href="#">198</a>	J222235.8-324528	335.6493	-32.7577	-	-	71.3 ± 8.3	82.1 ± 8.0	80.7 ± 10.7	-	-	3.39	2.73	13.50
<a href="#">199</a>	J133352.2+334913	203.4674	33.8203	19.0	-18.05	112.4 ± 5.4	108.8 ± 5.9	80.6 ± 7.0	18.4 ± 9.7	-	2.01	2.22	13.25
<a href="#">200</a>	J014313.2-332633	25.8052	-33.4425	-9.04	20.05	107.1 ± 6.1	109.7 ± 6.0	80.5 ± 7.5	21.5 ± 11.0	-	2.19	2.33	13.30
<a href="#">201</a>	J141117.8-010655	212.8246	-1.1155	1.97	3.02	52.2 ± 7.2	78.6 ± 8.2	80.5 ± 8.7	39.4 ± 9.4	-	4.00	3.31	13.58
<a href="#">202</a>	J143328.4+020811	218.3684	2.1365	-5.9	4.03	117.5 ± 7.3	100.7 ± 8.3	80.4 ± 8.5	35.7 ± 8.4	-	2.02	2.05	13.26
<a href="#">203</a>	J141827.4-001703	214.6145	-0.2843	5.53	-19.01	117.2 ± 6.5	116.4 ± 7.4	80.2 ± 7.6	22.0 ± 10.6	-	2.01	2.13	13.27
<a href="#">204</a>	J132909.5+300957	202.2896	30.1658	-	-	57.9 ± 5.5	95.3 ± 6.1	80.1 ± 7.1	-	-	4.18	3.01	13.67
<a href="#">205</a>	J145132.7+024101	222.8866	2.6837	-6.1	1.98	84.5 ± 7.2	104.4 ± 8.3	80.2 ± 8.9	45.5 ± 10.5	-	3.01	2.67	13.48
<a href="#">206</a>	J140421.7-001217	211.0907	-0.2048	0.43	1.96	79.3 ± 7.4	102.6 ± 8.4	80.2 ± 8.8	32.2 ± 10.1	-	2.94	2.72	13.44
<a href="#">207</a>	J005506.5-300027	13.777	-30.0076	-6.0	-0.01	96.9 ± 5.9	121.7 ± 6.1	80.2 ± 7.5	41.8 ± 9.7	-	2.60	2.77	13.42
<a href="#">208</a>	J225744.6-324231	344.4358	-32.7086	-	-	69.4 ± 5.1	91.9 ± 5.5	80.1 ± 6.6	-	-	3.60	2.85	13.56
<a href="#">209</a>	J224920.6-332940	342.3358	-33.4944	-	-	85.6 ± 6.0	102.6 ± 6.3	80.1 ± 7.5	-	-	2.90	2.59	13.45

Table A2: Blazars - SPIRE and SCUBA-2 data. The blazar index hyperlinks to the NED database at the position of the source. These sources have been removed from the HerBS sample in Section 2. The RA and DEC are the SPIRE-positions,  $\Delta$ RA and  $\Delta$ DEC are the SPIRE positions minus the SCUBA-2 positions. The spectroscopic redshifts are discussed in Section 4. The  $\alpha$  value defines the steepness of the slope of the synchrotron radiation, and is calculated in Section 2.

No.	H-ATLAS ID	RA [hms]	DEC [dms]	$\Delta$ RA ["]	$\Delta$ DEC ["]	S <sub>250</sub> [mJy]	S <sub>350</sub> [mJy]	S <sub>500</sub> [mJy]	S <sub>850</sub> [mJy]	$z_{\text{spec}}$	$\alpha$
-----	------------	-------------	--------------	--------------------	---------------------	---------------------------	---------------------------	---------------------------	---------------------------	-------------------	----------

<sup>1</sup> This source is also in Negrello's sample

<sup>2</sup> The 850 micron flux of this source was re-evaluated

Table A2: Blazars - SPIRE and SCUBA-2 data. The blazar index hyperlinks to the NED database at the position of the source. These sources have been removed from the HerBS sample in Section 2. The RA and DEC are the SPIRE-positions,  $\Delta$ RA and  $\Delta$ DEC are the SPIRE positions minus the SCUBA-2 positions. The spectroscopic redshifts are discussed in Section 4. The  $\alpha$  value defines the steepness of the slope of the synchrotron radiation, and is calculated in Section 2.

No.	H-ATLAS ID	RA [hms]	DEC [dms]	$\Delta$ RA ["]	$\Delta$ DEC ["]	S <sub>250</sub> [mJy]	S <sub>350</sub> [mJy]	S <sub>500</sub> [mJy]	S <sub>850</sub> [mJy]	z <sub>spec</sub>	$\alpha$
1	J131028.7+322044	197.6197	32.3455	-2.06	2.05	259.1 ± 4.4	363.1 ± 5.1	452.2 ± 6.1	820.0 ± 6.0	1.0	0.93 ± 0.01
2	J114637.9-001132	137.2924	1.3597	-0.52	-0.03	256.5 ± 3.8	327.0 ± 4.5	375.3 ± 6.0	390.7 ± 7.7	1.02	0.32 ± 0.01
3	J014503.4-273333	26.264	-27.5591	-0.67	0.98	131.5 ± 5.7	179.1 ± 6.3	233.5 ± 7.2	365.8 ± 6.7	1.16	0.83 ± 0.02
4	J083051.0+013225	194.4888	32.4918	-2.12	3.03	143.7 ± 5.1	188.4 ± 5.7	214.9 ± 6.7	290.0 ± 7.6	0.81	0.54 ± 0.02
5	J224838.6-323551	342.1608	-32.5974	-1.18	2.99	119.2 ± 5.5	152.8 ± 5.8	194.8 ± 6.7	173.5 ± 7.2	2.27	0.24 ± 0.03
6	J121758.7-002946	184.4947	-0.4961	-2.62	1.01	115.7 ± 5.3	151.5 ± 5.7	179.2 ± 6.6	206.7 ± 7.2	0.42	0.44 ± 0.03
7	J014310.0-320056	25.7917	-32.0157	-2.38	4.0	96.0 ± 5.3	119.5 ± 5.9	122.4 ± 7.2	405.6 ± 8.5	0.38	1.02 ± 0.04
8	J084933.4+021442	203.2808	27.4217	-5.76	1.01	89.3 ± 5.3	104.6 ± 5.5	117.1 ± 6.4	128.5 ± 10.4	2.13	0.3 ± 0.05
9	J131736.4+342518	199.4017	34.4217	0.21	6.06	77.1 ± 5.1	99.5 ± 5.5	112.0 ± 6.8	129.0 ± 7.8	1.06	0.39 ± 0.05
10	J113526.2-014606	358.4476	-30.6294	-2.06	3.99	77.1 ± 5.1	96.6 ± 5.8	103.1 ± 7.0	143.9 ± 8.1	1.06	0.48 ± 0.05
11	J132952.9+315410	202.4703	31.9027	-2.92	-1.0	50.5 ± 5.2	71.0 ± 5.5	86.4 ± 7.3	253.4 ± 7.8	0.34	1.27 ± 0.06
12	J235935.3-313343	359.8972	-31.5621	-4.16	5.04	61.4 ± 5.5	67.7 ± 5.8	83.7 ± 7.4	117.3 ± 8.6	0.99	0.54 ± 0.06
13	J142413.9+022303	177.6818	-0.3985	-1.4	5.98	34.5 ± 5.3	56.1 ± 5.5	83.2 ± 6.7	187.9 ± 9.3	1.98	1.37 ± 0.07
14	J131059.2+323331	197.7467	32.5587	7.4	2.03	37.6 ± 5.3	63.2 ± 5.7	81.7 ± 6.5	313.7 ± 7.8	1.64	1.67 ± 0.07

**APPENDIX B: CUTOUPS OF THE ENTIRE HERBS SAMPLE**

This paper has been typeset from a  $\text{\TeX/L\AA\TeX}$  file prepared by the author.

